



# Geochronology, geochemistry, and petrogenesis of I- and A-type granites in the Solwezi Dome of the Lufilian Arc: implications for the late-Mesoproterozoic magmatic and geodynamic evolution in northern Zambia

Kang-kang Xu<sup>1,2</sup> · Wei Xie<sup>3</sup> · Kai Sun<sup>1,2</sup> · Jun-ping Ren<sup>1,2</sup> · Peng-hui Gong<sup>1,2</sup> · Sheng-fei He<sup>1,2</sup> · Yi-guan Lu<sup>1,2</sup> · Hang Zhang<sup>1,2</sup>

Received: 31 March 2022 / Accepted: 29 October 2022 / Published online: 28 November 2022  
© Saudi Society for Geosciences 2022

## Abstract

The late-Mesoproterozoic granitoids, which were discovered for the first time in the Solwezi Dome of the Lufilian Arc, can provide pivotal constraints on the provenance of detrital materials in the Neoproterozoic Katanga Supergroup and the reconstruction of the Mesoproterozoic continent. We report here U–Pb zircon ages, geochemical and Sr–Nd–Hf isotopic data for the gneissic K-feldspar granite and the gneissic biotite monzogranite in the Solwezi Dome, northern Zambia. Mineralogical and geochemical features suggest that the K-feldspar granite and the biotite monzogranite are I- and A-type, respectively. LA-MC-ICP-MS zircon U–Pb analyses yield an age of  $1178 \pm 15$  Ma for the K-feldspar granite, and consistent ages ranging from  $1105 \pm 7$  to  $1109 \pm 7$  Ma for two samples from the biotite monzogranite. The K-feldspar granites, having aluminous to weak peraluminous, low calculated zircon saturation temperatures ( $771 \sim 806^\circ\text{C}$ ), high Sr/Y ratios ( $17.32 \sim 46.19$ ) and initial  $^{87}\text{Sr}/^{86}\text{Sr}$  ratios ( $0.7162 \sim 0.7217$ ), and negative zircon  $\epsilon_{\text{Nd}}(t)$  ( $-9.17 \sim -9.24$ ) and  $\epsilon_{\text{Hf}}(t)$  ( $-12.03 \sim -7.10$ ), were derived by partial melting of Neoarchean basement in a slightly thickened lower crust. The biotite monzogranites have high Nb, Ce, Zr, Y, and Ga/Al ratios, high calculated zircon saturation temperatures ( $836 \sim 902^\circ\text{C}$ ), relatively flat HREE patterns [ $(\text{Gd}/\text{Yb})_N = 3.38 \sim 5.76$ ], obviously negative Eu anomalies ( $\delta\text{Eu} = 0.28 \sim 0.45$ ), low Sr/Y ratios ( $4.87 \sim 13.00$ ), high initial  $^{87}\text{Sr}/^{86}\text{Sr}$  ratios ( $0.7246 \sim 0.7305$ ), as well as negative  $\epsilon_{\text{Nd}}(t)$  ( $-8.67 \sim -9.98$ ) and zircon  $\epsilon_{\text{Hf}}(t)$  ( $-14.85 \sim -9.35$ ). They were likely generated by partial melting of Neoarchean basement in a relatively shallow depths. These 1178 Ma and  $1109 \sim 1105$  Ma I- and A-type granites in the Solwezi Dome were emplaced coeval with the widespread  $1.20 \sim 1.15$  Ga syntectonic granitoid and  $\sim 1100$  Ma post-tectonic bimodal igneous magmatism in the Choma-Kalomo Block, the Ghanzi-Chobe Belt, and the Namaqua Belt and so on. We think that these belts including the Lufilian Arc represent a buried southwestern continuation of the Kibaran Belt, and interpret these late-Mesoproterozoic granitoids as the igneous rocks formed during the syn-collisional and post-collisional stages of the Kibaran Orogen, respectively.

**Keywords** I- and A-type granite · Late-Mesoproterozoic · The Solwezi Dome · The Lufilian Arc · Northern Zambia

## Introduction

Responsible editor: Domenico M. Doronzo

✉ Kang-kang Xu  
xukang06@163.com

<sup>1</sup> Tianjin Center, China Geological Survey, Tianjin 300170, China

<sup>2</sup> North China Center of Geoscience Innovation, Tianjin 300170, China

<sup>3</sup> Tianjin Geological Mineral Testing Center, Tianjin 300191, China

Granitoids comprise significant portions of the continental crust; they display great variability in their sources, their association with tectonics, and their specific magma evolutionary processes; studying the processes involved in their generation may provide important clues to the growth and reworking of continental crust and to regional tectonics and geodynamic processes (Zhao et al. 2016; Goedde & Vervoort 2006; Heilimo et al. 2014; Kemp & Hawkesworth 2003; Ren et al. 2022; Sun et al. 2021). The granitoid can be

subdivided into S-, I-, M-, and A-type based on their chemical and mineralogical features (Barbarin 1999; Chappell & White 1992; Eby 1990; Loiselle and Wones 1979). Different magmatic assemblages are closely associated in space and time; these magmatism usually formed during the transition of tectonic regime, such as I- and A-type assemblages in the western margin of the Yangtze Block (Zhao et al. 2008), the Central Tianshan orogen (Dong et al. 2011), the Sanandaj-Sirjan Zone, NW Iran (Sarjoughian et al. 2016), and the Pataz gold-mining district in northern Peru (Witt et al. 2014).

The Lufilian Arc is known for its world-class sediment-host Cu–Co deposits which is located in central Africa (Cailteux et al. 2005; El Desouky et al. 2009; Hitzman et al. 2010; Key et al. 2001; Muchez et al. 2008; Eglinger et al. 2013). It is a large arcuate structure covering eastern Angola, the southern Democratic Republic of Congo, and northwestern Zambia (Katongo et al. 2004; Key et al. 2001; Batumike et al. 2006; Master et al. 2005). Geotectonically, the Lufilian Arc is located between the Congo Craton and the Kalahari Craton, and forms a part of a transcontinental network of Neoproterozoic-early Paleozoic orogenic belts in central-southern Africa together with the Zambezi Belt and the Damara Belt (Fig. 1(b)) (Katongo et al. 2004; Hanson et al. 1993; Dirks & Sithole 1999; Kampunzu & Cailteux 1999; Vinyu et al. 1999; Porada & Berhorst 2000). The Lufilian Arc is divided into five tectonic zones, which are the Plateau Foreland Basin, the External Fold and Thrust Belt, the Domes Region, the Synclinorial Belt, and the Katanga High from north to south (Fig. 1a) (De Swardt et al. 1965; Unrug 1983; Porada 1989; Kampunzu et al. 2000).

Regional investigations show that the Lufilian Arc underwent a phase of magmatic quiescence after the formation of Paleoproterozoic basement, which lasted until Neoproterozoic (Porada & Berhorst 2000; Key et al. 2001; Cosi et al. 1992; Hanson et al. 1994; Rainaud et al. 2005; Katongo et al. 2004). However, there are a substantial quantity of Mesoproterozoic detrital zircons developed in the belt, and the provenance of detrital zircons is controversial; most scholars believe that they are mainly derived from the surrounding Mesoproterozoic belt, such as the Kibaran Belt and the Irurrite Belt (Liu et al. 2019; Master et al. 2005). However, detrital zircons are generally sub-angular and exhibit clear fine oscillatory growth zoning, suggesting a magmatic origin and close detrital provenance (Liu et al. 2019; Xu et al. 2021). Furthermore, a large number of *ca.* 1.10 Ga detrital zircons developed in the Solwezi area have no corresponding magmatism in the Kibaran Belt. Thereby, Xu et al. (2021) speculate that they are mainly derived from the underlying basement. In addition, the absence of Mesoproterozoic magmatism in the Lufilian Arc makes it impossible to comparative study of magmatism with the surrounding terrains,

thus limiting the reconstruction of Mesoproterozoic supercontinent and adversely affecting the study of Precambrian geodynamics.

During the geological survey in the north of Zambia, we discovered Mesoproterozoic granitoids for the first time in the Solwezi Dome. Combining zircon U–Pb dating, whole-rock geochemical data, and Sr–Nd–Hf isotope analyses, this paper aims to address the following points: (1) the types and ages of granitoids, (2) petrogenesis and tectonic setting, (3) source of Mesoproterozoic detrital materials and tectonic significance represented by granitoids in the Lufilian Arc.

## Geological setting

The Domes Region is characterized by the occurrence of basement inliers defining an arcuate chain parallel to the trend of folds developed during the Lufilian Pan African orogeny (Kampunzu et al. 2000). The study area is mainly located in the Solwezi Dome, where the basement and the Neoproterozoic Katanga Supergroup are developed (Fig. 2).

The basement is composed of the Lufubu schists and gneisses, which are intruded by the Eburnian (*ca.* 2200 ~ 1800 Ma) granites (Key et al. 2001; Rainaud et al. 2005). The Lufubu schists are usually calc-alkaline and formed as a result of the subduction of oceanic lithosphere between 2.1 and 1.8 Ga (Rainaud et al. 2005). The Mesoproterozoic magmatism had not previously been identified until the present geological survey, and the Nchanga Granite is the youngest intrusion in the pre-Katangan basement with a zircon U–Pb age of  $883 \pm 10$  Ma (Armstrong et al. 2005; Master et al. 2005).

The Neoproterozoic Katanga Supergroup which unconformably overlies the basement is consisted of a *ca.* 10,000-m-thick sequence of sedimentary and metasedimentary rocks; it can be divided into the Roan Group, the Nugba Group, the Kundelungu Group, and the Biano Group from bottom to top (Cailteux 1994; Cailtrux et al. 2007; Batumike et al. 2007; Cailteux & Putter 2019). The Roan Group contains important Cu–Co mineralization (Armstrong et al. 2005; Master et al. 2005); it is characterized by basement gravels and detrital materials with overlying carbonates interbedded with shales; the Mwashya Subgroup at the top is composed of black shales and dolomitic siltstones. The stratigraphic succession shows that the sedimentary hydrodynamic environment changed from shallow to deep (Cailteux 1994; Cailteux et al. 2005). The Nguba and Kundelungu groups are two sedimentary sequences having diamictites at the bottom with overlying carbonates, followed by predominantly siliciclastic sedimentary rocks at the top (Batumike et al. 2006, 2007). The Biano Group occurs at the top of the Katanga succession, which is a continental clastic molasse-type deposit consisting of coarse to fine-grained arkoses and intraclastic conglomerates (Cailteux & Putter 2019).

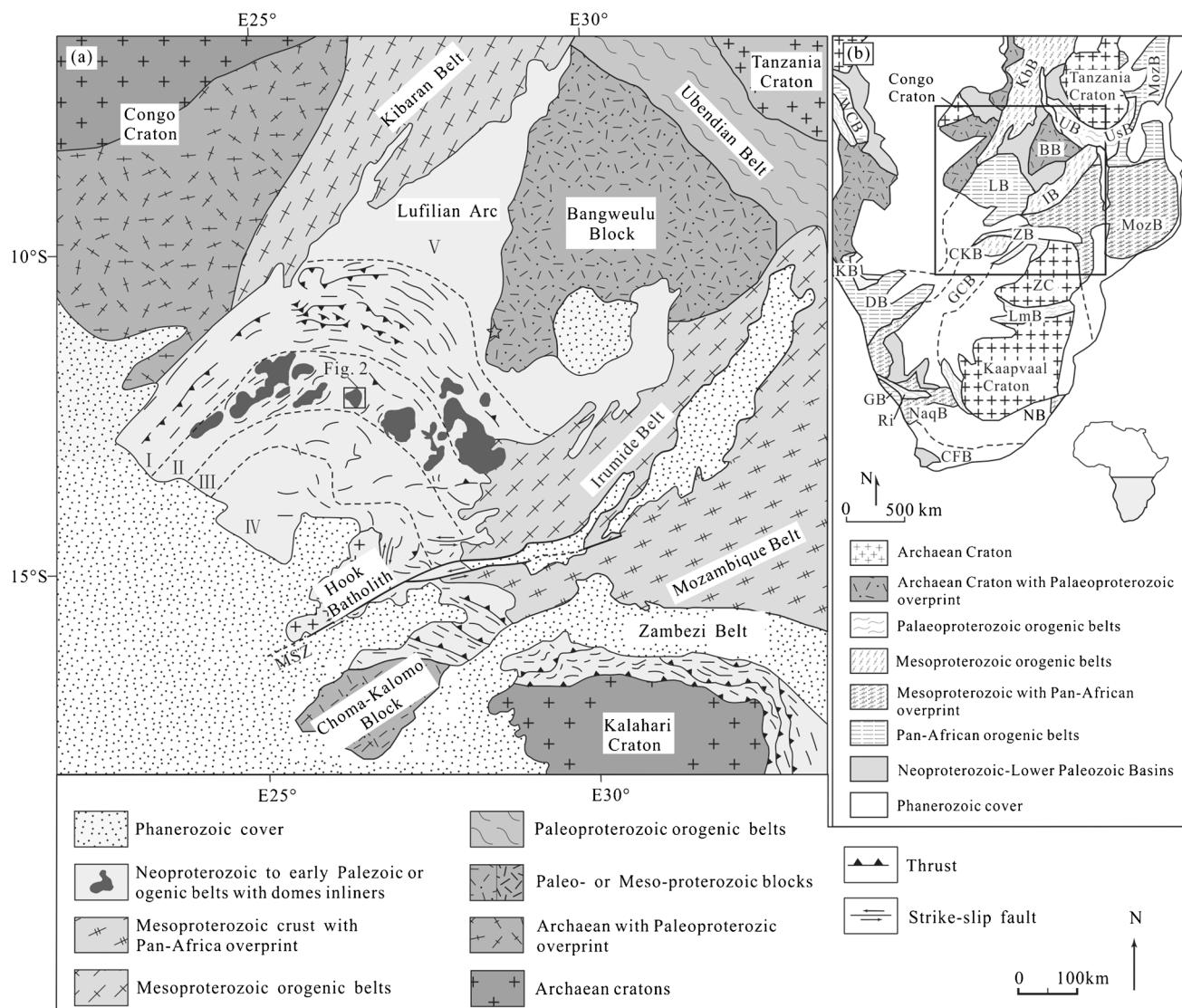


**Fig. 1** Simplified geological map of central-southern Africa showing the distribution of tectonic features discussed in text (modified from Eglinger et al. 2016; Johnson et al. 2005). BB, Bangweulu Block; CFB, Cape Fold Belt; CKB, Choma-Kalomo Block; DB, Damara Belt; GB, Garip Belt; GCB, Ghanzi-Chobe Belt; IB, Irumide Belt; KB, Kaoko Belt; KbB, Kibaran Belt; KhB, Kheis Belt; LB, Lufilian

Belt; LmB, Limpopo Belt; MozB, Mozambique Belt; NaqB, Namaqua Belt; NB, Natal Belt; Ri, Richtersveld Terrane; UB, Ubendian Belt; UsB, Usagaran Belt; WCB, West Congo Belt; ZB, Zambezi Belt; ZC, Zimbabwe Craton; I-External Fold and Thrust Belt; II-Domes Region; III-Synclinorial Belt; IV-Kantanga High; V-Foreland Basin

At the late stage of sedimentation, the Katanga Supergroup was deformed by the Lufilian orogeny as a consequence of an interaction between the Congo Craton and the Kalahari Craton; metamorphic assemblages are principally in the greenschist facies, but higher grades up to eclogite facies have been locally recorded (Porada & Berhorst 2000; Naydenov et al. 2014; Rainaud et al. 2005). Eclogite facies metamorphism from Central Zambia yielded a Sm-Nd isochron at  $595 \pm 10$  Ma, and records the timing of the subduction which took place in an oceanic environment (John et al. 2003). While a phase of high-pressure whiteschist metamorphism yielded a U-Pb monazite age of  $529 \pm 2$  Ma, it

represents the final stage of the collision between the Congo and the Kalahari cratons (John et al. 2004).

## Petrography

The granitic complex is located in the northeastern part of the Solwezi Dome, which is funnel-shaped with an area of about  $35\text{km}^2$  (Fig. 2). The complex intruded into the Lufubu schists with the Katanga Supergroup unconformably overlaid in the north. It exhibits typical granitic characteristics with some minerals extending roughly N-S or NW-SE because of later regional tectonics (Fig. 3a, b). The complex

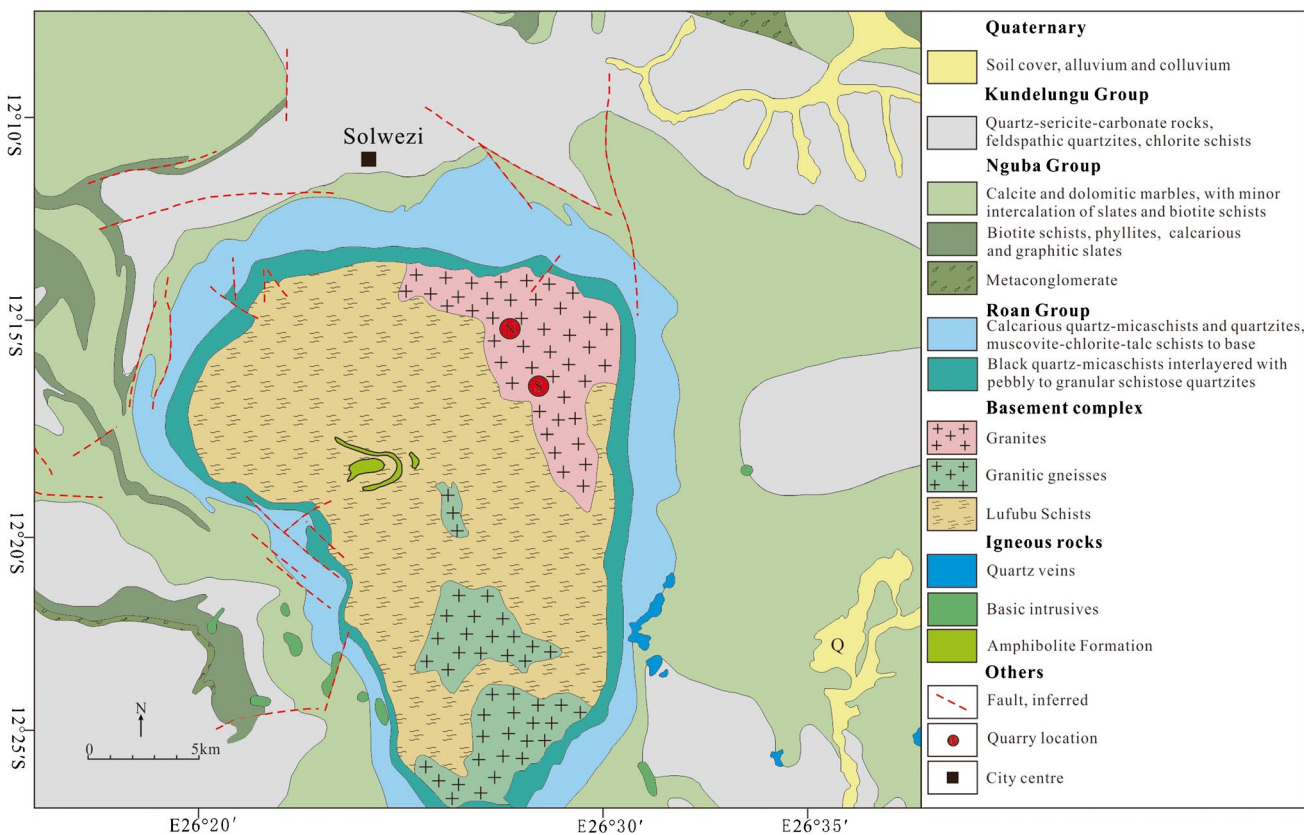


**Fig. 2** Simplified map showing the distribution of granitoids in Solwezi area (modified from Johnson et al. 2005; Selley et al. 2005)

is mainly composed of the gneissic K-feldspar granite and the gneissic biotite monzogranite; the latter often occurs copper mineralization (Fig. 3c, d). The contact relationship between them has not been detected owing to the extensive coverage of the study area. The dating samples of the K-feldspar granite (ZS50) and the biotite monzogranites (ZS29, ZS30) are collected from the northern quarry and the southern quarry, respectively. The sample list and corresponding GPS coordinates are given in Table 1.

The K-feldspar granites are pink with porphyritic texture and massive/gneissic structure. The minerals are mainly composed of the K-feldspar (40%), plagioclase (25%), quartz (25%), and biotite (4%) as well as a small amount of accessory minerals including zircon, apatite, and Fe-Ti oxide, etc. (6%). The K-feldspars are long columnar with Carlsbad twinning, and some appear as microcline with weakly sericitized and kaolinitized. The plagioclases show albite twin with weakly sericitized. The biotites are flaky and typically along the boundaries between the K-feldspars and plagioclases, suggesting they are late crystallization phases (Fig. 3e).

The biotite monzogranites are gray with porphyritic texture and massive/gneissic structure. The minerals are mainly composed of the K-feldspar (35%), plagioclase (30%), quartz

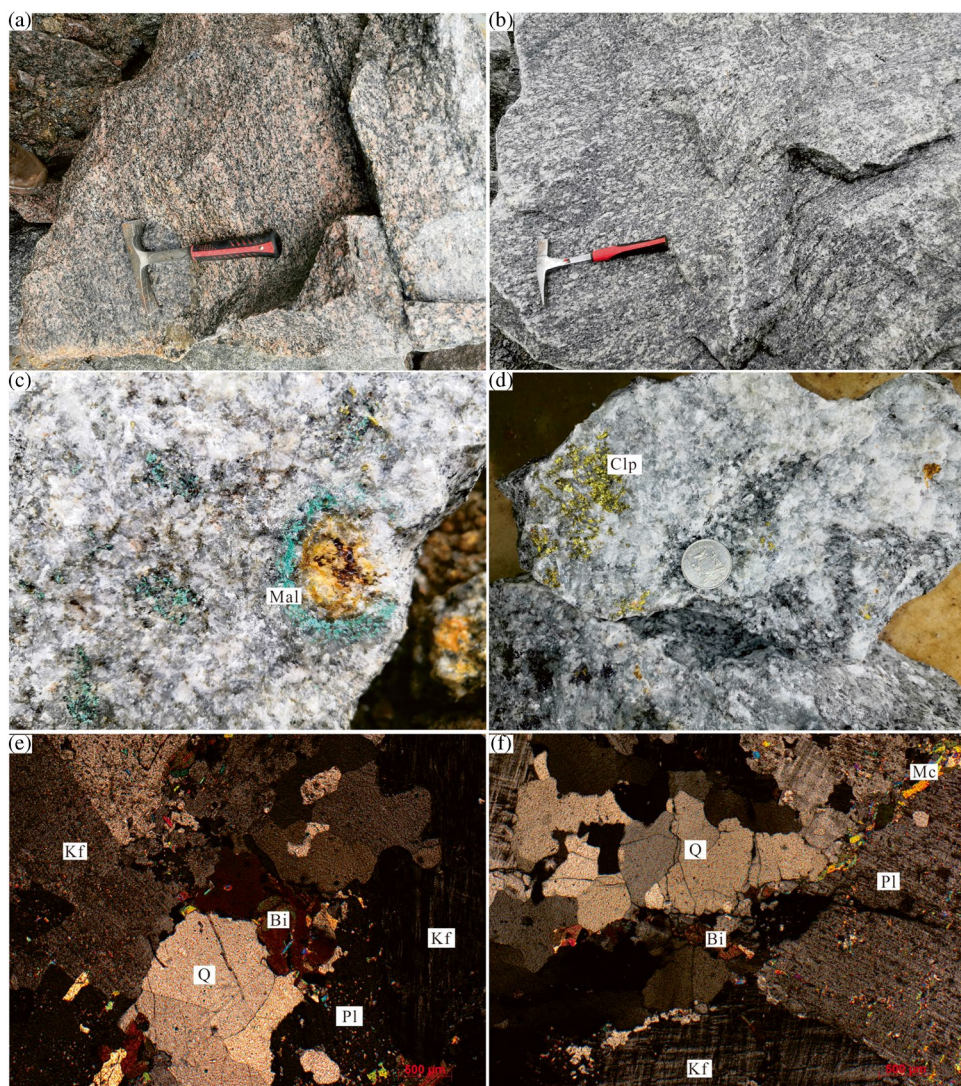
(20%), biotite (8%), and muscovite (2%) and a small amount of accessory minerals including zircon, apatite, and Fe-Ti oxide, etc. (5%). The K-feldspars are long columnar with Carlsbad or crossed twinning. The plagioclases show albite twin and are weakly sericitized. The quartz and biotites are often filled between the feldspars, indicating that they are also late crystallization phases (Fig. 3f).

## Analytical methods

### LA-MC-ICP-MS zircon U-Pb dating

Zircons were separated by using standard density and magnetic separation techniques and then random zircon grains were handpicked under a binocular microscope at the Yu'neng Geological and Mineral Separation Survey Centre of Langfang, Hebei Province, China. Zircons were mounted in epoxy in a 1.4-cm diameter circular grain mount and then polished to section the crystals in half for analysis at the GeoAnalysis CO. Ltd., Beijing. Meanwhile, transmitted and reflected light images and cathodoluminescence (CL) images were made at the same laboratory, using a JXA-8800 R electron microprobe and a JXA-8800 R electron

**Fig. 3** Photographs of the outcrops and photomicrographs of the K-feldspar granite and the biotite monzogranite in the Solwezi Dome. **a** The gneissic K-feldspar granite; **b** the gneissic biotite monzogranite; **c**, **d** mineralized biotite monzogranite; **e**, **f** photomicrographs showing mineral assemblages and textural characteristics of the K-feldspar granite (ZS45) and the biotite monzogranite (ZS34), respectively. Clp: Chalcopyrite; Mal: Malachite; Kf: K-feldspar; Pl: Plagioclase; Mc: Microcline; Bi: Biotite; Q: Quartz



microprobe, respectively. Lastly, zircon U–Pb analyses were conducted on an Agilent 7500a ICP-MS equipped with a New Wave Research laser-ablation system at Institute of Geology and Mineral Resources in Tianjin, China (TIGMR). The laser system delivered a beam of 193-nm UV light from a frequency-quintupled Neptune instrument (Thermo Fisher Company). Analyses were carried out with a beam diameter of 35  $\mu\text{m}$ , a repetition rate of 8–10 Hz, and an energy of 10–11 J/cm<sup>2</sup>. Data acquisition for each analysis took 20 s for the background and 40 s for the signal. Zircon 91,500 and silica glass NIST610 were used as external standards for optimizing instruments. An Excel-based software ICP-MS-Data-Cal was used to perform offline selection and integration of background and analyzed signals, time-drift correction, and quantitative calibration for trace element analysis and U–Pb dating (Liu et al. 2008, 2010a, b). Concordia diagrams and weighted mean age calculations were made using ISOPLOT 4.15 software (Ludwig 2003).

### Zircon Lu–Hf isotopic analyses

The in situ Lu–Hf isotopes were analyzed on the same spots or in adjacent domains of zircon grains with similar texture where U–Pb dating was done at TIGMR, following analytical techniques described by Yuan et al. (2004). The energy density of 15~20 J/cm<sup>2</sup> and a spot diameter of 50  $\mu\text{m}$  are used in this study. GJ-1 was used as the reference standard, with a weighted mean  $^{176}\text{Hf}/^{177}\text{Hf}$  ratio of  $0.282004 \pm 46$  ( $2\sigma$ ,  $n=31$ ) during our routine analyses. In this study, the decay constant of  $^{176}\text{Lu}$  of  $1.865 \times 10^{-11}/\text{a}$  was adopted (Scherer et al. 2001). Initial  $^{176}\text{Hf}/^{177}\text{Hf}$  ratios and  $\epsilon_{\text{Hf}}(t)$  values were calculated with reference to the chondritic reservoir of Blichert-Toft and Albarède (1997). The depleted-mantle Hf model age ( $T_{\text{DM1}}$ ) was calculated with present-day  $^{176}\text{Hf}/^{177}\text{Hf}$  (0.28325) and  $^{176}\text{Lu}/^{177}\text{Lu}$  (0.0384) values (Griffin et al. 2000). Two-stage “crustal” model ages

**Table 1** Sample locations and corresponding coordinates (WGS 84)

Sample	Lithology	Location	S	E
ZS44	K-feldspar granite	Northern quarry	12°15'23.14"	26°27'49.56"
ZS45	K-feldspar granite	Northern quarry	12°15'21.17"	26°27'49.69"
ZS46	K-feldspar granite	Northern quarry	12°15'21.80"	26°27'50.30"
ZS48	K-feldspar granite	Northern quarry	12°15'23.04"	26°27'51.57"
ZS49	K-feldspar granite	Northern quarry	12°15'23.53"	26°27'51.53"
ZS50	K-feldspar granite	Northern quarry	12°15'22.81"	26°27'51.09"
ZS51	K-feldspar granite	Northern quarry	12°15'23.92"	26°27'50.67"
ZS52	K-feldspar granite	Northern quarry	12°15'23.77"	26°27'50.39"
ZS25	Biotite monzogranite	Southern quarry	12°16'28.53"	26°28'20.27"
ZS26	Biotite monzogranite	Southern quarry	12°16'28.11"	26°28'19.50"
ZS27	Biotite monzogranite	Southern quarry	12°16'29.23"	26°28'20.26"
ZS28	Biotite monzogranite	Southern quarry	12°16'28.86"	26°28'19.76"
ZS29	Biotite monzogranite	Southern quarry	12°16'29.71"	26°28'20.59"
ZS30	Biotite monzogranite	Southern quarry	12°16'30.36"	26°28'18.37"
ZS31	Biotite monzogranite	Southern quarry	12°16'29.51"	26°28'18.10"
ZS32	Biotite monzogranite	Southern quarry	12°16'28.97"	26°28'17.95"
ZS33	Biotite monzogranite	Southern quarry	12°16'28.22"	26°28'18.11"
ZS34	Biotite monzogranite	Southern quarry	12°16'28.01"	26°28'18.66"

( $T_{DM2}$ ) were calculated for the average continental crust with a  $^{176}\text{Lu}/^{177}\text{Hf}$  ratio of 0.015 (Griffin et al. 2002).

### Whole-rock geochemical analyses

For major, trace and rare earth element analyses, the rocks were reduced in a jaw crusher and then powdered to 200 mesh at the Yu'neng Laboratory. Whole-rock major elements were identified by using a PW4400/40 X-ray fluorescence spectrometer at Tianjin Institute of Geology and Mineral Resources (TIGMR), Tianjin. The contents of  $\text{Fe}_2\text{O}_3$  and FeO were analyzed through conventional wet chemistry and titration. The analytical precision is generally better than 2% for all the major elements. Trace element and rare earth element (REE) abundances were measured by using an X Series II ICP-MS at TIGMR with analytical precisions better than 5%. The detailed analytical procedure followed that of Gao et al. (2003).

### Whole-rock Sr–Nd isotopic analyses

Samples used for Rb–Sr and Sm–Nd isotope analysis were spiked with mixed isotope tracers, dissolved 7 days in teflon capsules using HF,  $\text{HClO}_4$ , and  $\text{HNO}_3$  acids, and separated by conventional cation-exchange techniques (AG50×12). Isotopic measurements were performed using a FinniganTritonTi thermal ionization mass spectrometer at the TIGMR. Procedural blanks yielded concentrations of <200 pg for Sm and Nd, and <500 pg for Rb and Sr. Mass fractionation corrections for Sr and Nd isotopic ratios were based on  $^{88}\text{Sr}/^{86}\text{Sr} = 8.375209$  and  $^{146}\text{Nd}/^{144}\text{Nd} = 0.7219$ ,

respectively, and analysis of the NBS987 and LRIG standards yielded values of  $^{87}\text{Sr}/^{86}\text{Sr} = 0.710245 \pm 30$  ( $2\sigma$ ) and  $^{143}\text{Nd}/^{144}\text{Nd} = 0.512202 \pm 30$  ( $2\sigma$ ), respectively.

The  $\varepsilon_{\text{Nd}}(t)$  values and Nd model ages were calculated assuming  $^{147}\text{Sm}/^{144}\text{Nd}$  and  $^{143}\text{Nd}/^{144}\text{Nd}$  ratios for average chondrite and the depleted mantle at the present day to be 0.1967 and 0.512638, and 0.2137 and 0.51315, respectively (Hamilton et al. 1983; Goldstein et al. 1984). Here,  $\lambda\text{Rb}$  and  $\lambda\text{Sm}$  are  $1.42 \times 10^{-11}$  year $^{-1}$  and  $6.54 \times 10^{-12}$  year $^{-1}$ , respectively (Lugmair & Hart 1978).

## Analytical results

### Zircon U–Pb age

The U–Pb isotopic data of the K-feldspar granites (ZS50) and the biotite monzogranites (ZS29 and ZS30) are listed in Table 2.

### The K-feldspar granite

The majority of zircons collected from ZS50 are euhedral-subhedral with lengths and length/width ratios ranging from 80 to 200  $\mu\text{m}$  and 2:1 to 3:1, respectively. Visible oscillatory zoning in cathodoluminescence (CL) images (Fig. 4a) and high Th/U ratios (usually >0.1) indicate a magmatic origin of these zircons (Hoskin & Schaltegger 2000). However, the disruption of oscillatory zoning and development of irregular domains of homogenous can be observed locally due to later metamorphism; therefore, the least severely affected

**Table 2** LA-MC-ICP-MS zircon U-Pb dating results of the late-Mesoproterozoic granitoids in the Solwezi Dome

Spot no	Contents (ppm)	Th/U		Ratios		207Pb/235U		206Pb/238U		Ages (Ma)							
		Th	U	207Pb/206Pb	1σ	207Pb/235U	1σ	206Pb/238U	1σ	207Pb/206Pb	1σ	206Pb/238U	1σ	Concordia			
ZS50																	
ZS50-01	119	392	0.30	0.0791		0.0022	2.0636	0.0552	0.1879	0.0019	1181	51	1138	17	1110	9	97%
ZS50-02	47	377	0.12	0.1067		0.0026	3.9562	0.1036	0.2665	0.0036	1744	44	1625	21	1523	18	94%
ZS50-03	116	434	0.27	0.0780		0.0031	1.3787	0.0427	0.1272	0.0021	1120	116	870	18	770	12	88%
ZS50-04	138	803	0.17	0.0804		0.0018	1.9942	0.0474	0.1789	0.0024	1176	55	1160	21	1146	23	99%
ZS50-05	36.437	1187	30.70	0.0789		0.0043	1.4102	0.0341	0.1310	0.0015	1129	118	884	15	798	9	90%
ZS50-06	188	2227	0.08	0.0779		0.0040	1.3380	0.0335	0.1311	0.0022	1218	101	885	15	790	13	89%
ZS50-07	194	458	0.42	0.0785		0.0022	1.6876	0.0494	0.1552	0.0024	1191	61	1162	20	1140	13	98%
ZS50-08	67	2636	0.03	0.0779		0.0064	1.4320	0.0494	0.1353	0.0019	1187	154	911	20	814	11	89%
ZS50-09	115	297	0.39	0.0771		0.0020	1.9742	0.0539	0.1841	0.0024	1166	48	1153	18	1140	12	99%
ZS50-10	132	1650	0.08	0.0766		0.0038	1.4658	0.0414	0.1449	0.0019	1200	83	939	14	859	12	91%
ZS50-11	83	957	0.09	0.0763		0.0016	1.8931	0.0579	0.1781	0.0042	1110	9	1143	19	1151	22	99%
ZS50-12	291	494	0.59	0.0775		0.0017	1.9733	0.0420	0.1834	0.0017	1165	46	1155	14	1143	10	99%
ZS50-13	305	553	0.55	0.0789		0.0022	1.6161	0.0384	0.1478	0.0015	1099	148	1004	22	957	12	95%
ZS50-14	221	523	0.42	0.0780		0.0017	1.9465	0.0463	0.1794	0.0023	1198	52	1164	21	1138	23	98%
ZS50-15	252	298	0.85	0.0779		0.0026	1.7828	0.0516	0.1659	0.0022	1140	38	1002	23	935	13	93%
ZS50-16	1096	2426	0.45	0.1537		0.0045	0.8113	0.0186	0.0398	0.0010	2375	49	604	10	253	6	18%
ZS50-17	17	467	0.04	0.0795		0.0021	2.0877	0.0481	0.1898	0.0022	1161	54	1146	17	1131	12	99%
ZS50-18	172	349	0.49	0.0800		0.0021	2.2087	0.0586	0.1985	0.0018	1184	52	1170	18	1152	10	98%
ZS50-19	407	260	1.57	0.0787		0.0022	1.7531	0.0470	0.1601	0.0015	1169	52	1030	16	959	8	93%
ZS50-20	133	259	0.51	0.0787		0.0022	1.8989	0.0522	0.1735	0.0017	1146	50	1082	17	1043	9	96%
ZS50-21	255	307	0.83	0.0799		0.0024	2.1095	0.0568	0.1909	0.0021	1194	55	1152	19	1126	12	98%
ZS50-22	163	303	0.54	0.0767		0.0030	1.6916	0.0659	0.1585	0.0022	1115	78	1005	25	948	12	94%
ZS50-23	137	1691	0.08	0.0614		0.0041	1.5751	0.0422	0.1487	0.0026	654	144	960	17	893	15	93%
ZS50-24	234	433	0.54	0.0767		0.0029	1.8267	0.0701	0.1713	0.0031	1114	76	1055	25	1019	17	97%
ZS50-25	348	1212	0.29	0.1081		0.0033	1.7848	0.0480	0.1203	0.0020	1769	50	1040	18	733	11	65%
ZS50-26	288	307	0.94	0.0777		0.0030	1.8034	0.0674	0.1677	0.0027	1139	76	1047	24	1000	15	95%
ZS50-27	431	631	0.68	0.0778		0.0030	1.8323	0.0596	0.1699	0.0028	1140	77	1057	21	1011	16	96%
ZS50-28	26	965	0.03	0.0800		0.0030	2.1193	0.0720	0.1901	0.0042	1198	76	1155	23	1122	23	97%
ZS50-29	103	829	0.12	0.0772		0.0044	1.4458	0.0399	0.1332	0.0042	1126	113	908	17	806	24	88%
ZS50-30	244	403	0.61	0.0728		0.0024	1.8354	0.0588	0.1805	0.0020	1009	66	1058	21	1070	11	99%
ZS50-31	116	829	0.14	0.0771		0.0039	1.6354	0.0556	0.1552	0.0023	1124	101	984	21	930	13	94%
ZS50-32	283	464	0.61	0.0788		0.0031	1.9256	0.0651	0.1756	0.0027	1169	78	1090	23	1043	15	96%
ZS50-33	195	447	0.44	0.0802		0.0025	2.1179	0.0624	0.1891	0.0021	1267	61	1155	20	1116	11	97%
ZS50-34	240	424	0.57	0.0791		0.0036	1.4692	0.0480	0.1334	0.0017	1176	91	918	20	807	10	87%
ZS50-35	216	373	0.58	0.0772		0.0025	1.5228	0.0525	0.1411	0.0026	1128	65	940	21	851	15	90%

**Table 2** (continued)

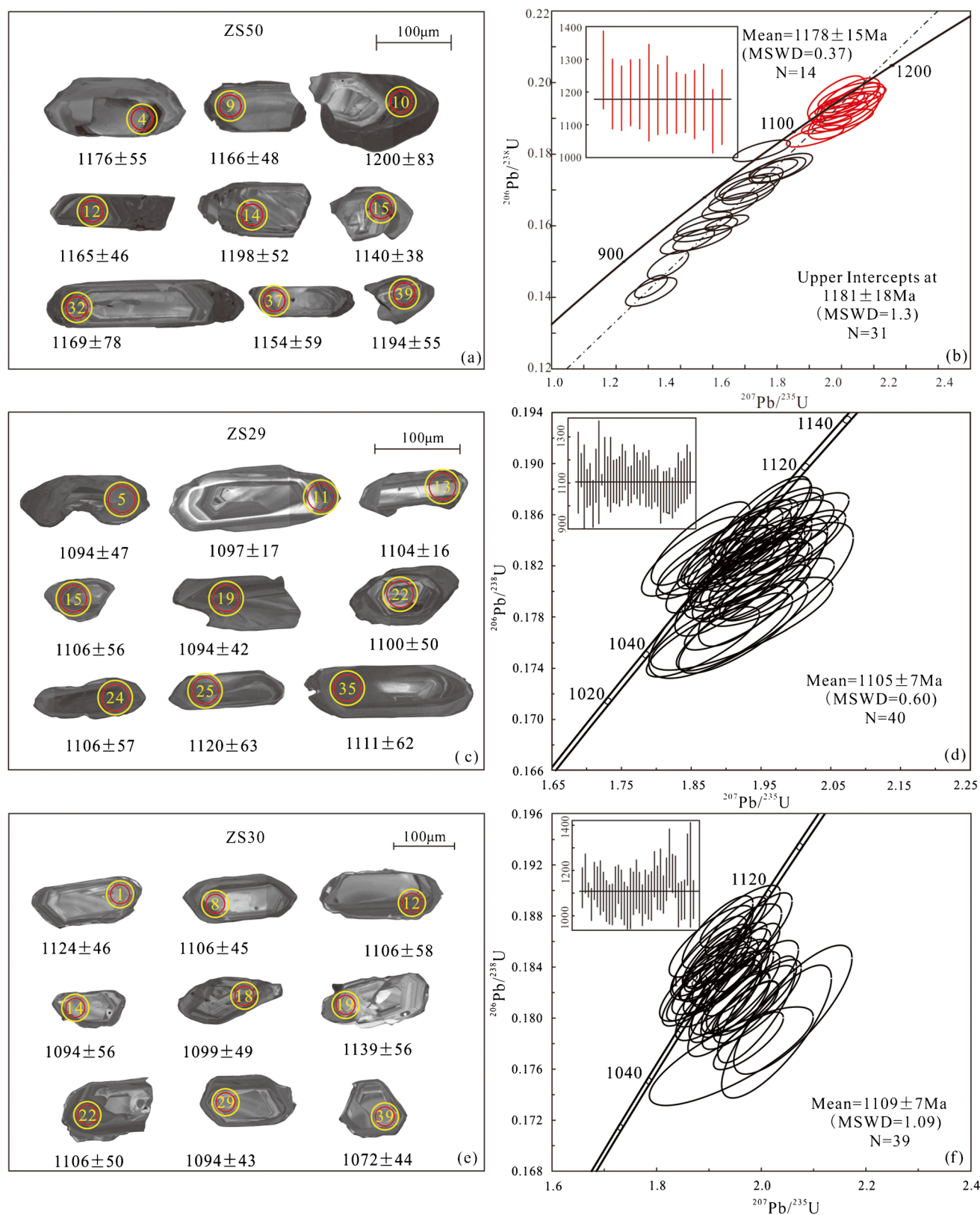
Spot no	Contents (ppm)	Th/U	Ratios			Ages (Ma)										
			$^{207}\text{Pb}/^{206}\text{Pb}$	$1\sigma$	$^{207}\text{Pb}/^{235}\text{U}$	$1\sigma$	$^{206}\text{Pb}/^{238}\text{U}$	$1\sigma$	$^{207}\text{Pb}/^{206}\text{Pb}$	$1\sigma$	$^{206}\text{Pb}/^{235}\text{U}$	$1\sigma$	$^{206}\text{Pb}/^{238}\text{U}$	$1\sigma$	Concordia	
ZS50-36	271	560	0.48	0.0762	0.0022	1.8134	0.0524	0.1704	0.0021	1102	58	1050	19	1015	12	97%
ZS50-37	171	295	0.58	0.0782	0.0023	2.1347	0.0618	0.1959	0.0025	1154	59	1160	20	1153	13	99%
ZS50-38	395	520	0.76	0.0794	0.0030	1.9190	0.0554	0.1752	0.0023	1183	75	1088	19	1040	13	96%
ZS50-39	212	404	0.53	0.0799	0.0024	2.0536	0.0588	0.1846	0.0020	1194	55	1133	20	1092	11	96%
ZS50-40	365	325	1.12	0.0770	0.0025	1.7676	0.0574	0.1652	0.0024	1120	65	1034	21	986	13	95%
ZS29																
ZS29-01	707	334	2.12	0.0779	0.0023	1.9846	0.0573	0.1833	0.0020	1144	91	1110	20	1085	11	98%
ZS29-02	10	637	0.02	0.0783	0.0017	1.9977	0.0418	0.1836	0.0015	1155	38	1115	14	1087	8	97%
ZS29-03	187	472	0.40	0.0756	0.0035	1.9285	0.0834	0.1834	0.0025	1084	93	1091	29	1086	13	100%
ZS29-04	33	432	0.08	0.0753	0.0016	1.9355	0.0388	0.1850	0.0014	1076	43	1093	13	1094	8	100%
ZS29-05	15	765	0.02	0.0759	0.0017	1.9576	0.0429	0.1853	0.0023	1094	47	1101	15	1096	13	100%
ZS29-06	8	495	0.02	0.0728	0.0019	1.8534	0.0491	0.1827	0.0021	1009	53	1065	17	1082	11	98%
ZS29-07	51	464	0.11	0.0774	0.0023	1.9602	0.0560	0.1818	0.0020	1131	60	1102	19	1077	11	98%
ZS29-08	296	312	0.95	0.0780	0.0045	1.9358	0.0667	0.1793	0.0040	1146	115	1094	33	1063	22	97%
ZS29-09	18	659	0.03	0.0767	0.0017	1.9605	0.0414	0.1834	0.0016	1114	13	1102	14	1085	9	98%
ZS29-10	248	169	1.47	0.0788	0.0026	1.9529	0.0610	0.1807	0.0033	1169	67	1099	21	1071	18	97%
ZS29-11	55	441	0.12	0.0764	0.0019	1.9472	0.0500	0.1826	0.0017	1106	56	1097	17	1081	9	98%
ZS29-12	129	477	0.27	0.0776	0.0033	1.9226	0.0862	0.1775	0.0024	1136	84	1089	30	1053	13	97%
ZS29-13	324	289	1.12	0.0764	0.0018	1.9676	0.0454	0.1850	0.0018	1106	48	1104	16	1094	10	99%
ZS29-14	155	640	0.24	0.0764	0.0019	1.9302	0.0518	0.1812	0.0023	1106	50	1092	18	1073	13	98%
ZS29-15	162	438	0.37	0.0764	0.0021	1.9312	0.0541	0.1817	0.0022	1106	56	1092	19	1077	12	99%
ZS29-16	51	677	0.07	0.0780	0.0025	1.9247	0.0611	0.1772	0.0024	1146	63	1090	21	1052	13	96%
ZS29-17	21	871	0.02	0.0782	0.0017	1.9581	0.0415	0.1799	0.0014	1154	44	1101	14	1066	8	97%
ZS29-18	29	623	0.05	0.0756	0.0017	1.9520	0.0452	0.1856	0.0022	1085	44	1099	16	1098	12	100%
ZS29-19	44	598	0.07	0.0760	0.0016	1.9409	0.0412	0.1841	0.0021	1094	42	1095	14	1089	11	99%
ZS29-20	26	425	0.06	0.0784	0.0023	1.9655	0.0591	0.1799	0.0018	1158	56	1104	20	1067	10	97%
ZS29-21	91	669	0.14	0.0774	0.0020	1.9144	0.0489	0.1779	0.0016	1131	52	1086	17	1056	9	97%
ZS29-22	331	472	0.70	0.0758	0.0019	1.9088	0.0542	0.1803	0.0025	1100	50	1084	19	1069	14	99%
ZS29-23	106	641	0.16	0.0778	0.0018	1.9477	0.0436	0.1803	0.0017	1143	46	1098	15	1069	9	97%
ZS29-24	19	468	0.04	0.0764	0.0022	1.9576	0.0539	0.1851	0.0020	1106	57	1101	19	1095	11	99%
ZS29-25	645	505	1.28	0.0770	0.0024	1.9299	0.0589	0.1810	0.0021	1120	63	1092	20	1072	11	98%
ZS29-26	216	687	0.31	0.0752	0.0016	1.9054	0.0399	0.1826	0.0016	1072	44	1083	14	1081	9	100%
ZS29-27	43	733	0.06	0.0757	0.0016	1.9094	0.0393	0.1815	0.0015	1088	37	1084	14	1075	8	99%
ZS29-28	142	577	0.25	0.0756	0.0018	1.9196	0.0487	0.1826	0.0026	1087	46	1088	17	1081	14	99%
ZS29-29	17	580	0.03	0.0729	0.0017	1.8634	0.0467	0.1837	0.0021	1013	46	1068	17	1087	12	98%

Table 2 (continued)

Spot no	Contents (ppm)	Th/U	Ratios			Ages (Ma)								
			$^{207}\text{Pb}/^{206}\text{Pb}$	$1\sigma$	$^{207}\text{Pb}/^{235}\text{U}$	$1\sigma$	$^{206}\text{Pb}/^{238}\text{U}$	$1\sigma$	$^{207}\text{Pb}/^{206}\text{Pb}$	$1\sigma$	$^{206}\text{Pb}/^{235}\text{U}$	$1\sigma$	$^{206}\text{Pb}/^{238}\text{U}$	
ZS29-30	237	469	0.50	0.0747	0.0017	1.8951	0.0427	0.1830	0.0019	1061	46	1079	15	1084
ZS29-31	120	376	0.32	0.0748	0.0017	1.8786	0.0427	0.1813	0.0020	1062	46	1074	15	1074
ZS29-32	151	525	0.29	0.0749	0.0018	1.9044	0.0456	0.1829	0.0015	1066	51	1083	16	1083
ZS29-33	30	492	0.06	0.0737	0.0016	1.8626	0.0414	0.1817	0.0015	1035	46	1068	15	1076
ZS29-34	358	382	0.94	0.0751	0.0018	1.9107	0.0466	0.1834	0.0021	1070	49	1085	16	1086
ZS29-35	517	485	1.07	0.0766	0.0023	1.8670	0.0535	0.1761	0.0018	1111	62	1069	19	1045
ZS29-36	10	591	0.02	0.0763	0.0018	1.9450	0.0452	0.1832	0.0017	1102	48	1097	16	1084
ZS29-37	8	474	0.02	0.0766	0.0019	1.9333	0.0466	0.1814	0.0018	1109	50	1093	16	1075
ZS29-38	34	433	0.08	0.0780	0.0024	1.9122	0.0550	0.1769	0.0020	1148	61	1085	19	1050
ZS29-39	300	371	0.81	0.0779	0.0018	1.9573	0.0439	0.1808	0.0020	1144	47	1101	15	1071
ZS29-40	135	323	0.42	0.0775	0.0021	1.9977	0.0518	0.1850	0.0018	1144	54	1115	18	1094
ZS30														
ZS30-1	308	441	0.70	0.0771	0.0018	1.9555	0.0397	0.1825	0.0023	1124	46	1100	14	1081
ZS30-2	126	246	0.51	0.0796	0.0018	1.9756	0.0441	0.1782	0.0015	1187	45	1107	15	1057
ZS30-3	443	556	0.80	0.0767	0.0017	1.9733	0.0411	0.1847	0.0018	1114	17	1106	14	1093
ZS30-4	35	564	0.06	0.0743	0.0014	1.9050	0.0342	0.1841	0.0014	1050	37	1083	12	1090
ZS30-5	40	797	0.05	0.0782	0.0017	1.9691	0.0414	0.1808	0.0014	1154	43	1105	14	1071
ZS30-6	183	428	0.43	0.0772	0.0018	1.9569	0.0440	0.1828	0.0017	1128	46	1101	15	1082
ZS30-7	8	705	0.01	0.0771	0.0022	1.9510	0.0559	0.1820	0.0022	1124	62	1099	19	1078
ZS30-8	135	562	0.24	0.0764	0.0017	1.9318	0.0461	0.1817	0.0024	1106	45	1092	16	1076
ZS30-9	134	152	0.88	0.0748	0.0017	1.9086	0.0434	0.1837	0.0016	1065	47	1084	15	1087
ZS30-10	8	648	0.01	0.0743	0.0015	1.9059	0.0367	0.1848	0.0015	1050	45	1083	13	1093
ZS30-11	12	237	0.05	0.0743	0.0016	1.8794	0.0397	0.1821	0.0015	1050	47	1074	14	1078
ZS30-12	171	216	0.79	0.0764	0.0022	1.9184	0.0542	0.1812	0.0020	1106	58	1088	19	1074
ZS30-13	28	669	0.04	0.0777	0.0017	1.9500	0.0432	0.1810	0.0017	1139	44	1098	15	1073
ZS30-14	152	127	1.20	0.0760	0.0021	1.9170	0.0533	0.1820	0.0017	1094	56	1087	19	1078
ZS30-15	239	417	0.57	0.0745	0.0018	1.8806	0.0462	0.1821	0.0018	1054	49	1074	16	1079
ZS30-16	143	203	0.71	0.0737	0.0020	1.9041	0.0528	0.1860	0.0018	1035	49	1083	18	1100
ZS30-17	163	298	0.54	0.0752	0.0025	1.9328	0.0700	0.1852	0.0025	1076	69	1093	24	1095
ZS30-18	212	315	0.67	0.0761	0.0019	1.9196	0.0451	0.1827	0.0016	1099	49	1088	16	1082
ZS30-19	158	299	0.53	0.0777	0.0021	1.9384	0.0518	0.1803	0.0022	1139	56	1094	18	1069
ZS30-20	17	478	0.04	0.0762	0.0018	1.9429	0.0495	0.1839	0.0020	1102	47	1096	17	1088
ZS30-21	14	544	0.03	0.0742	0.0017	1.9166	0.0445	0.1867	0.0019	1047	47	1087	16	1104
ZS30-22	72	185	0.39	0.0763	0.0019	1.9390	0.0500	0.1836	0.0017	1106	50	1095	17	1087
ZS30-23	7	248	0.03	0.0904	0.0037	2.3655	0.0779	0.1895	0.0027	1435	78	1232	24	1119

**Table 2** (continued)

Spot no	Contents (ppm)	Th/U		Ratios		Ages (Ma)										
		Th	U	$^{207}\text{Pb}/^{206}\text{Pb}$	$1\sigma$	$^{207}\text{Pb}/^{235}\text{U}$	$1\sigma$	$^{206}\text{Pb}/^{238}\text{U}$	$1\sigma$	$^{207}\text{Pb}/^{206}\text{Pb}$	$1\sigma$	$^{206}\text{Pb}/^{235}\text{U}$	$1\sigma$	$^{206}\text{Pb}/^{238}\text{U}$	$1\sigma$	Concordia
ZS30-24	93	148	0.63	0.0755	0.0019	1.9597	0.0504	0.1880	0.0016	1083	51	1102	17	1110	9	99%
ZS30-25	106	104	1.02	0.0757	0.0021	1.9096	0.0529	0.1829	0.0017	1087	56	1084	18	1083	9	100%
ZS30-26	17	193	0.9	0.0795	0.0021	1.9926	0.0553	0.1813	0.0022	1183	52	1113	19	1074	12	96%
ZS30-27	114	112	1.01	0.0771	0.0019	1.9850	0.0488	0.1866	0.0021	1124	50	1110	17	1103	11	99%
ZS30-28	182	525	0.35	0.0785	0.0028	1.9784	0.0612	0.1824	0.0024	1161	70	1108	21	1080	13	97%
ZS30-29	27	242	0.11	0.0759	0.0017	1.9467	0.0423	0.1851	0.0016	1094	43	1097	15	1095	9	100%
ZS30-30	13	459	0.03	0.0785	0.0019	1.9603	0.0482	0.1802	0.0018	1161	49	1102	17	1068	10	97%
ZS30-31	473	332	1.42	0.0824	0.0028	2.0604	0.0746	0.1807	0.0033	1254	67	1136	25	1071	18	94%
ZS30-32	176	613	0.29	0.0796	0.0018	1.9921	0.0497	0.1807	0.0028	1187	44	1113	17	1071	15	96%
ZS30-33	18	173	0.11	0.0790	0.0019	1.9899	0.0483	0.1815	0.0017	1173	48	1112	16	1075	9	97%
ZS30-34	240	150	1.60	0.0742	0.0018	1.9009	0.0467	0.1849	0.0021	1047	50	1081	16	1093	11	99%
ZS30-35	128	666	0.19	0.0749	0.0016	1.9178	0.0410	0.1848	0.0017	1066	44	1087	14	1093	9	99%
ZS30-36	8	507	0.02	0.0751	0.0015	1.9517	0.0385	0.1872	0.0015	1072	45	1099	13	1106	8	99%
ZS30-37	13	703	0.02	0.0821	0.0025	2.0292	0.0692	0.1789	0.0034	1248	59	1125	23	1061	19	94%
ZS30-38	11	710	0.02	0.0794	0.0046	1.9429	0.1034	0.1770	0.0025	1181	119	1096	36	1051	14	96%
ZS30-39	179	182	0.98	0.0752	0.0018	1.9132	0.0450	0.1842	0.0019	1072	44	1086	16	1090	10	100%
ZS30-40	308	322	0.96	0.0754	0.0026	1.9000	0.0622	0.1830	0.0022	1080	70	1081	22	1083	12	100%



**Fig. 4** Cathodoluminescence (CL) images for representative zircons (**a, c, e**) and U–Pb concordia diagrams for zircons (**b, d, f**) from the granitoids in the Solwezi Dome

zircon domains are chosen during the analysis to avoid getting a “mixed” isotopic ages (Corfu & Hanchar 2003).

Forty analyses were conducted on thirty-nine zircons, one inherited zircon with an old age of  $1744 \pm 44$  Ma, and eight zircons with a low concordant degree (< 90%) were rejected; the remaining thirty-one analyses yield a discordant line with an upper intercept at  $1181 \pm 18$  Ma ( $\text{MSWD} = 1.3$ ), fourteen analyses of which give a weighted mean  $^{207}\text{Pb}/^{206}\text{Pb}$  age of  $1178 \pm 15$  Ma ( $\text{MSWD} = 0.37$ ) (Fig. 4b), interpreted as crystallization age of the K-feldspar granite.

### The biotite monzogranite

Zircons collected from ZS29 and ZS30 are euhedral-subhedral with lengths and length/width ratios ranging from 60 to 210  $\mu\text{m}$  and 2:1 to 3:1, respectively (Fig. 4c, e). The CL images show that zircons mostly have visible oscillatory zoning, and their Th/U ratios are 0.02~2.12 and 0.01~1.60, respectively, which support their magmatic origin and later weakly partial metamorphism (Rubatto 2017).

Forty analyses were conducted on forty zircons of ZS29, yielding concordant  $^{207}\text{Pb}/^{206}\text{Pb}$  ages of  $1009 \sim 1169$  Ma, with a weighted mean age of  $1105 \pm 7$  Ma ( $\text{MSWD} = 0.60$ ) (Fig. 4d), interpreted as crystallization age of the biotite monzogranite. Forty analyses were conducted on thirty-nine zircons of ZS30, except for one zircon (23) with an old age of  $1435 \pm 78$  Ma, the remaining thirty-nine analyses yield concordant  $^{207}\text{Pb}/^{206}\text{Pb}$  ages of  $1035 \sim 1254$  Ma, with a weighted mean age of  $1109 \pm 7$  Ma ( $\text{MSWD} = 1.09$ ) (Fig. 4f), which is compatible with ZS29 within the error.

### Zircon Lu–Hf isotopic data

Zircons from the three samples dated by U–Pb were also analyzed for their Lu–Hf isotopes on the same domains (but a larger range), and the results are listed in Table 3 and illustrated in Fig. 5a. The  $^{176}\text{Lu}/^{177}\text{Hf}$  ratios of all the zircons are less than 0.002, indicating that there is no significant accumulation of radiogenic Hf following zircon crystallization (Patchett et al. 1982).

Thirty-seven analyses were obtained for ZS50, and the crystallization age of 1178 Ma was used for the calculation of  $\varepsilon_{\text{Hf}}(t)$  and  $T_{\text{DM}}$  values, yielding  $\varepsilon_{\text{Hf}}(t)$  values between  $-12.03$  and  $-7.10$ , corresponding to  $T_{\text{DM1}}$  model ages between 1989 and 2168 Ma and  $T_{\text{DM2}}$  model ages between 2423 and 2728 Ma.

Twenty-nine analyses were obtained for ZS29, and the crystallization age of 1105 Ma was used for the calculation of  $\varepsilon_{\text{Hf}}(t)$  and  $T_{\text{DM}}$  values, yielding  $\varepsilon_{\text{Hf}}(t)$  values between  $-14.85$  and  $-9.99$ , corresponding to  $T_{\text{DM1}}$  model ages between 2017 and 2214 Ma and  $T_{\text{DM2}}$  model ages between 2547 and 2847 Ma.

Thirty analyses were obtained for ZS30, and the crystallization age of 1109 Ma was used for the calculation of  $\varepsilon_{\text{Hf}}(t)$  and  $T_{\text{DM}}$  values, yielding  $\varepsilon_{\text{Hf}}(t)$  values between  $-13.06$  and  $-9.35$ , corresponding to  $T_{\text{DM1}}$  model ages between 1983 and 2224 Ma and  $T_{\text{DM2}}$  model ages between 2511 and 2740 Ma.

### Major and trace elements

The data of major and trace elements for the K-feldspar granites and the biotite monzogranites are listed in Table 4.

### Alteration and element mobility

As the Solwezi granitoids had suffered deformation and greenschist facies metamorphism, it is imperative to ascertain if metamorphism may have led to significant post-emplacement element mobility that may preclude use of compositional data to make petrogenetic inferences. All the samples have low loss on ignition values (0.70~1.22%), and the chemical indices of alteration of 43.6~52.5 are comparable to those of unaltered granite (50, Nesbitt & Young 1982; Katongo et al. 2004), implying that all the samples have rarely been affected by later metamorphism and alteration. The high field strength elements (HFSEs) and REEs are immobile during secondary processes whereas the large ion lithophile elements (LILEs) are considered mobile (Polat & Hofmann 2003). The Solwezi granitoids were assessed for post-emplacement alteration by plotting Zr (a known sensitive indicator of immobility) against REE (represented by La), HFSE (represented by Nb), and LILE (represented by Sr) as well as some major elements ( $\text{K}_2\text{O}$ ,  $\text{Na}_2\text{O}$ , and  $\text{Al}_2\text{O}_3$ ) (Fig. 6). The results show that all elements have a good correlation with Zr, suggesting that the HFSE, the REE, the LILE, and the major elements were not significantly affected by post-emplacement processes, thus allowing their use for purposes of drawing petrogenetic inferences.

### The K-feldspar granite

The K-feldspar granites have variable contents of  $\text{SiO}_2$  (71.5~73.1 wt%),  $\text{FeO}_t$  ( $\text{FeO} + 0.8998 \times \text{Fe}_2\text{O}_3$ ) (1.62~2.08 wt%),  $\text{CaO}$  (0.92~1.11 wt%),  $\text{TiO}_2$  (0.20~0.27 wt%), and  $\text{P}_2\text{O}_5$  (0.066~0.11 wt%). The  $\text{MgO}$  contents are 0.43~0.65 wt% and  $\text{Mg}^{\#}$  values are 30~39. CIPW-normative compositions indicate that they have compositions similar to monzogranite (Fig. 7a). Their  $\text{K}_2\text{O}$  and  $\text{Na}_2\text{O}$  contents are 6.04~6.26 wt% and 2.59~3.12 wt%, respectively, with  $\text{K}_2\text{O}/\text{Na}_2\text{O}$  ratios of 1.31~2.41, mainly falling in the field of sub-alkaline granites on the TAS diagram (Fig. 7b) and the high-K calc-alkaline series on the  $\text{K}_2\text{O}$  vs.  $\text{SiO}_2$  diagram (Fig. 7c). They are metaluminous to weak peraluminous

**Table 3** Zircon in situ Lu–Hf isotope data of the late-Mesoproterozoic granitoids in the Solwezi Dome

w	Age(Ma)	$^{176}\text{Yb}/^{177}\text{Hf}$	$2\sigma$	$^{176}\text{Lu}/^{177}\text{Hf}$	$2\sigma$	$^{176}\text{Hf}/^{177}\text{Hf}$	$2\sigma$	$\epsilon\text{Hf}(t)$	$2\sigma$	T <sub>DM1</sub>	$2\sigma$	T <sub>DM2</sub>	$2\sigma$
<b>ZS50</b>													
ZS50-1	1178	0.0359	0.0009	0.0013	0.0000	0.281746	0.000015	-11.22	0.85	2128	22	2678	38
ZS50-2	1178	0.0346	0.0009	0.0012	0.0000	0.281839	0.000015	-7.88	0.84	1996	21	2471	37
ZS50-3	1178	0.0495	0.0004	0.0019	0.0000	0.281775	0.000015	-10.67	0.83	2122	21	2644	37
ZS50-4	1178	0.0361	0.0010	0.0010	0.0000	0.281769	0.000016	-10.18	0.88	2080	23	2614	40
ZS50-5	1178	0.0649	0.0008	0.0018	0.0000	0.281754	0.000017	-11.31	0.87	2144	23	2684	40
ZS50-6	1178	0.0609	0.0020	0.0017	0.0000	0.281812	0.000017	-9.17	0.88	2057	24	2551	41
ZS50-7	1178	0.0363	0.0012	0.0012	0.0000	0.281787	0.000015	-9.70	0.85	2067	21	2584	38
ZS50-8	1178	0.0504	0.0012	0.0018	0.0000	0.281760	0.000016	-11.09	0.85	2135	22	2670	39
ZS50-9	1178	0.0426	0.0009	0.0013	0.0000	0.281742	0.000017	-11.34	0.89	2132	24	2686	41
ZS50-10	1178	0.0262	0.0011	0.0008	0.0000	0.281798	0.000017	-8.96	0.88	2028	23	2539	41
ZS50-11	1178	0.0458	0.0016	0.0014	0.0000	0.281850	0.000016	-7.61	0.86	1989	22	2455	39
ZS50-12	1178	0.0673	0.0013	0.0023	0.0000	0.281799	0.000015	-10.12	0.83	2110	22	2610	37
ZS50-13	1178	0.0376	0.0007	0.0013	0.0000	0.281756	0.000015	-10.85	0.83	2114	20	2655	36
ZS50-14	1178	0.0458	0.0004	0.0014	0.0000	0.281810	0.000017	-9.06	0.89	2047	24	2544	42
ZS50-15	1178	0.0229	0.0004	0.0008	0.0000	0.281789	0.000013	-9.30	0.80	2041	18	2559	34
ZS50-16	1178	0.0742	0.0018	0.0024	0.0000	0.281887	0.000020	-7.10	0.94	1991	28	2423	47
ZS50-17	1178	0.0457	0.0003	0.0017	0.0000	0.281793	0.000013	-9.90	0.79	2087	18	2597	33
ZS50-18	1178	0.0450	0.0002	0.0014	0.0000	0.281807	0.000017	-9.16	0.89	2050	24	2551	42
ZS50-19	1178	0.0386	0.0002	0.0012	0.0000	0.281815	0.000017	-8.70	0.89	2028	24	2523	42
ZS50-20	1178	0.0309	0.0004	0.0011	0.0000	0.281748	0.000015	-10.98	0.84	2113	21	2664	38
ZS50-21	1178	0.0294	0.0009	0.0010	0.0000	0.281776	0.000018	-9.93	0.92	2070	25	2598	44
ZS50-22	1178	0.0230	0.0006	0.0007	0.0000	0.281784	0.000017	-9.38	0.88	2042	23	2564	41
ZS50-23	1178	0.0459	0.0005	0.0016	0.0000	0.281731	0.000015	-12.03	0.84	2169	21	2728	38
ZS50-24	1178	0.0374	0.0005	0.0013	0.0000	0.281795	0.000016	-9.49	0.87	2060	23	2571	40
ZS50-25	1178	0.0367	0.0008	0.0015	0.0000	0.281806	0.000015	-9.22	0.83	2054	20	2554	36
ZS50-26	1178	0.0141	0.0005	0.0005	0.0000	0.281733	0.000017	-11.01	0.91	2099	24	2666	42
ZS50-27	1178	0.0503	0.0009	0.0019	0.0000	0.281787	0.000016	-10.22	0.85	2103	23	2616	39
ZS50-28	1178	0.0420	0.0003	0.0016	0.0000	0.281784	0.000015	-10.10	0.83	2091	21	2609	36
ZS50-29	1178	0.0513	0.0014	0.0018	0.0000	0.281792	0.000019	-9.98	0.94	2091	27	2601	46
ZS50-30	1178	0.0522	0.0002	0.0020	0.0000	0.281812	0.000016	-9.43	0.84	2074	22	2567	38
ZS50-31	1178	0.0350	0.0006	0.0012	0.0000	0.281821	0.000017	-8.52	0.88	2021	24	2511	41
ZS50-32	1178	0.0326	0.0006	0.0011	0.0000	0.281765	0.000018	-10.36	0.92	2089	25	2625	44
ZS50-33	1178	0.0335	0.0013	0.0011	0.0000	0.281823	0.000016	-8.36	0.87	2012	23	2501	40
ZS50-34	1178	0.0439	0.0003	0.0015	0.0000	0.281798	0.000018	-9.57	0.90	2069	25	2576	42
ZS50-35	1178	0.0177	0.0005	0.0006	0.0000	0.281735	0.000014	-11.07	0.84	2105	20	2669	37
ZS50-36	1178	0.0378	0.0005	0.0014	0.0000	0.281767	0.000019	-10.56	0.93	2105	27	2637	45
ZS50-38	1178	0.0281	0.0003	0.0011	0.0000	0.281749	0.000016	-10.93	0.86	2111	22	2660	39
ZS50-39	1178	0.0231	0.0003	0.0008	0.0000	0.281729	0.000017	-11.44	0.88	2124	23	2692	40
ZS50-40	1178	0.0270	0.0004	0.0010	0.0000	0.281808	0.000015	-8.74	0.85	2024	21	2525	38
<b>ZS29</b>													
ZS29-1	1105	0.0345	0.0005	0.0012	0.0000	0.281808	0.000018	-10.54	0.71	2038	25	2581	41
ZS29-2	1105	0.0294	0.0006	0.0010	0.0000	0.281795	0.000015	-10.88	0.61	2047	21	2602	34
ZS29-3	1105	0.0217	0.0003	0.0007	0.0000	0.281754	0.000018	-12.07	0.70	2084	24	2676	40
ZS29-4	1105	0.0180	0.0005	0.0006	0.0000	0.281752	0.000018	-12.10	0.71	2084	25	2678	41
ZS29-5	1105	0.0379	0.0007	0.0013	0.0000	0.281742	0.000018	-12.97	0.70	2136	25	2731	40
ZS29-6	1105	0.0386	0.0020	0.0013	0.0000	0.281813	0.000020	-10.39	0.78	2033	28	2572	46
ZS29-7	1105	0.0190	0.0004	0.0006	0.0000	0.281699	0.000020	-13.93	0.76	2153	27	2791	44
ZS29-8	1105	0.0277	0.0002	0.0010	0.0000	0.281787	0.000015	-11.14	0.63	2056	21	2618	35
ZS29-9	1105	0.0332	0.0020	0.0013	0.0001	0.281824	0.000019	-9.99	0.75	2017	27	2547	44

**Table 3** (continued)

w	Age(Ma)	$^{176}\text{Yb}/^{177}\text{Hf}$	$2\sigma$	$^{176}\text{Lu}/^{177}\text{Hf}$	$2\sigma$	$^{176}\text{Hf}/^{177}\text{Hf}$	$2\sigma$	$\varepsilon\text{Hf}(t)$	$2\sigma$	$T_{\text{DM1}}$	$2\sigma$	$T_{\text{DM2}}$	$2\sigma$
ZS29-10	1105	0.0148	0.0002	0.0005	0.0000	0.281747	0.000016	-12.17	0.65	2083	22	2682	36
ZS29-12	1105	0.0462	0.0003	0.0015	0.0000	0.281692	0.000019	-14.85	0.75	2214	27	2847	43
ZS29-13	1105	0.0248	0.0002	0.0008	0.0000	0.281805	0.000017	-10.35	0.68	2021	23	2570	38
ZS29-14	1105	0.0321	0.0005	0.0012	0.0000	0.281787	0.000017	-11.25	0.68	2064	24	2625	38
ZS29-15	1105	0.0245	0.0006	0.0008	0.0000	0.281781	0.000018	-11.21	0.67	2055	23	2623	38
ZS29-16	1105	0.0351	0.0005	0.0012	0.0000	0.281789	0.000018	-11.20	0.72	2063	26	2622	41
ZS29-17	1105	0.0209	0.0001	0.0008	0.0000	0.281696	0.000017	-14.18	0.68	2167	23	2806	38
ZS29-18	1105	0.0244	0.0005	0.0008	0.0000	0.281778	0.000018	-11.30	0.69	2058	24	2628	39
ZS29-19	1105	0.0301	0.0003	0.0010	0.0000	0.281722	0.000017	-13.42	0.66	2145	23	2759	37
ZS29-20	1105	0.0276	0.0006	0.0010	0.0000	0.281727	0.000017	-13.23	0.68	2136	24	2748	39
ZS29-21	1105	0.0332	0.0008	0.0012	0.0000	0.281822	0.000017	-10.06	0.66	2020	23	2551	37
ZS29-22	1105	0.0174	0.0002	0.0006	0.0000	0.281725	0.000017	-13.01	0.68	2117	23	2734	39
ZS29-23	1105	0.0236	0.0001	0.0008	0.0000	0.281741	0.000014	-12.61	0.59	2108	20	2709	33
ZS29-24	1105	0.0264	0.0004	0.0009	0.0000	0.281780	0.000015	-11.32	0.60	2061	20	2629	33
ZS29-25	1105	0.0312	0.0002	0.0012	0.0000	0.281736	0.000017	-13.11	0.68	2139	24	2740	39
ZS29-26	1105	0.0220	0.0002	0.0008	0.0000	0.281743	0.000017	-12.51	0.69	2103	24	2703	39
ZS29-27	1105	0.0151	0.0002	0.0006	0.0000	0.281735	0.000015	-12.64	0.62	2102	21	2711	34
ZS29-28	1105	0.0197	0.0004	0.0007	0.0000	0.281785	0.000015	-10.94	0.62	2040	21	2606	34
ZS29-29	1105	0.0267	0.0013	0.0009	0.0000	0.281717	0.000017	-13.54	0.69	2146	24	2767	39
ZS29-30	1105	0.0227	0.0003	0.0007	0.0000	0.281741	0.000018	-12.57	0.72	2105	25	2707	41
ZS30													
ZS30-1	1109	0.0229	0.0002	0.0007	0.0000	0.281786	0.000019	-10.85	0.73	2041	26	2603	42
ZS30-2	1109	0.0290	0.0003	0.0009	0.0000	0.281774	0.000014	-11.45	0.58	2069	19	2640	32
ZS30-3	1109	0.0435	0.0014	0.0013	0.0000	0.281832	0.000018	-9.68	0.72	2010	26	2531	41
ZS30-5	1109	0.0244	0.0014	0.0007	0.0000	0.281829	0.000019	-9.35	0.75	1983	26	2511	43
ZS30-6	1109	0.0325	0.0009	0.0010	0.0000	0.281780	0.000016	-11.29	0.65	2065	23	2631	37
ZS30-7	1109	0.0269	0.0007	0.0011	0.0000	0.281796	0.000016	-10.79	0.63	2047	22	2600	35
ZS30-8	1109	0.0203	0.0001	0.0007	0.0000	0.281744	0.000016	-12.30	0.66	2095	22	2693	37
ZS30-9	1109	0.0313	0.0005	0.0009	0.0000	0.281779	0.000018	-11.27	0.69	2062	24	2629	39
ZS30-10	1109	0.0393	0.0010	0.0012	0.0000	0.281830	0.000016	-9.65	0.65	2006	22	2529	37
ZS30-11	1109	0.0239	0.0004	0.0008	0.0000	0.281782	0.000014	-11.07	0.60	2051	20	2617	33
ZS30-12	1109	0.0260	0.0005	0.0009	0.0000	0.281772	0.000017	-11.52	0.68	2073	24	2645	39
ZS30-13	1109	0.0309	0.0005	0.0011	0.0000	0.281800	0.000020	-10.65	0.78	2043	28	2591	45
ZS30-14	1109	0.0250	0.0001	0.0008	0.0000	0.281767	0.000017	-11.58	0.67	2071	23	2649	37
ZS30-15	1109	0.0203	0.0004	0.0007	0.0000	0.281736	0.000018	-12.58	0.71	2106	25	2710	41
ZS30-16	1109	0.0226	0.0005	0.0007	0.0000	0.281743	0.000018	-12.40	0.72	2101	25	2699	41
ZS30-17	1109	0.0355	0.0009	0.0013	0.0000	0.281828	0.000014	-9.78	0.59	2013	20	2537	33
ZS30-18	1109	0.0215	0.0001	0.0007	0.0000	0.281752	0.000017	-12.08	0.69	2088	24	2680	39
ZS30-19	1109	0.0146	0.0002	0.0005	0.0000	0.281738	0.000019	-12.40	0.73	2094	25	2699	42
ZS30-20	1109	0.0302	0.0004	0.0011	0.0000	0.281779	0.000016	-11.40	0.63	2072	22	2637	35
ZS30-21	1109	0.0288	0.0011	0.0010	0.0000	0.281817	0.000014	-9.99	0.60	2015	20	2550	33
ZS30-22	1109	0.0359	0.0003	0.0013	0.0000	0.281778	0.000017	-11.57	0.68	2083	24	2648	39
ZS30-23	1109	0.0216	0.0001	0.0007	0.0000	0.281790	0.000018	-10.73	0.72	2037	25	2596	41
ZS30-24	1109	0.0204	0.0001	0.0007	0.0000	0.281756	0.000018	-11.91	0.72	2081	25	2669	41
ZS30-25	1109	0.0311	0.0005	0.0011	0.0000	0.281747	0.000018	-12.57	0.72	2119	26	2710	41
ZS30-26	1109	0.0252	0.0002	0.0009	0.0000	0.281758	0.000016	-11.99	0.64	2089	22	2674	36
ZS30-27	1109	0.0194	0.0006	0.0006	0.0000	0.281722	0.000018	-13.06	0.71	2124	25	2740	41
ZS30-28	1109	0.0227	0.0003	0.0007	0.0000	0.281731	0.000018	-12.83	0.70	2117	24	2726	40
ZS30-29	1109	0.0270	0.0002	0.0009	0.0000	0.281781	0.000018	-11.15	0.72	2057	25	2622	41
ZS30-30	1109	0.0436	0.0004	0.0016	0.0000	0.281788	0.000017	-11.47	0.68	2089	24	2642	39

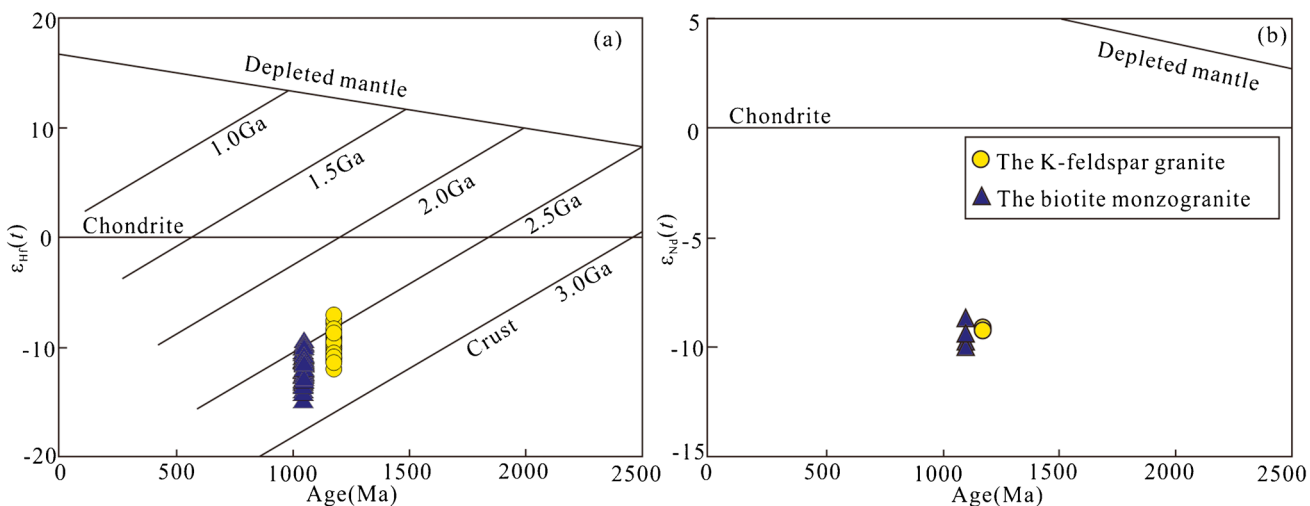


**Fig. 5**  $\epsilon_{\text{Hf}}(t)$  vs. zircon  $^{207}\text{Pb}/^{206}\text{Pb}$  age (a) and  $\epsilon_{\text{Nd}}(t)$  vs. U–Pb age (b) for the granitoids in the Solwezi Dome

( $\text{Al}_2\text{O}_3 = 13.4 \sim 14.4 \text{ wt\%}$ ,  $\text{A/CNK} = 0.84 \sim 1.06$ ) on the A/CNK vs. A/NK diagram (Fig. 7d).

They have high REE content of  $152 \sim 367 \text{ ppm}$ , and strongly fractionated REE patterns [ $(\text{La}/\text{Sm})_N = 3.99 \sim 4.63$ ,  $(\text{Gd}/\text{Yb})_N = 6.92 \sim 8.38$ ], as well as medium negative Eu anomalies ( $\delta\text{Eu} = 0.42 \sim 0.77$ ) (Fig. 8a). In the primitive mantle-normalized spidergram, they are characterized by enrichment in Rb, Th, K, U, and depletion in Ba, Nb, Ta, Sr, P, and Ti (Fig. 8b). Meanwhile, their Sr/Y ratios range from 17.3 to 46.2.

### The biotite monzogranite

Compared with the K-feldspar granite, the biotite monzogranites have higher  $\text{FeO}_t$  ( $2.58 \sim 4.95 \text{ wt\%}$ ),  $\text{CaO}$  ( $1.35 \sim 2.16 \text{ wt\%}$ ),  $\text{TiO}_2$  ( $0.44 \sim 0.91 \text{ wt\%}$ ),  $\text{P}_2\text{O}_5$  ( $0.23 \sim 0.36 \text{ wt\%}$ ),  $\text{MgO}$  ( $0.80 \sim 1.52 \text{ wt\%}$ ),  $\text{Na}_2\text{O}$  ( $2.68 \text{ wt\%} \sim 3.44 \text{ wt\%}$ ),  $\text{Mg}^{\#}$  ( $32 \sim 40$ ), and lower  $\text{SiO}_2$  ( $66.1 \sim 71.4 \text{ wt\%}$ ),  $\text{K}_2\text{O}$  ( $3.84 \sim 5.68 \text{ wt\%}$ ), and  $\text{K}_2\text{O}/\text{Na}_2\text{O}$  ratios ( $1.12 \sim 2.22$ ). CIPW-normative compositions are also similar to monzogranite (Fig. 7a). The majority of samples fall in the field of sub-alkaline granites (Fig. 7b) and the high-K calc-alkaline series (Fig. 7c). They are weak peraluminous ( $\text{Al}_2\text{O}_3 = 13.5 \sim 15.7 \text{ wt\%}$ ,  $\text{A/CNK} = 1.01 \sim 1.11$ ) (Fig. 7d).

Their REE contents are also high ( $371 \sim 667 \text{ ppm}$ ) and they are characterized by strongly fractionated LREE patterns [ $(\text{La}/\text{Sm})_N = 3.99 \sim 4.63$ ] and relatively flat HREE patterns [ $(\text{Gd}/\text{Yb})_N = 3.38 \sim 5.76$ ], as well as obviously negative Eu anomalies ( $\delta\text{Eu} = 0.28 \sim 0.45$ ) (Fig. 8c). In the primitive mantle-normalized spidergram, their geochemical characteristics are similar to the K-feldspar granites (Fig. 8d). The Sr/Y ratios ( $4.87 \sim 13.0$ ) are lower.

### Whole-rock Sr–Nd isotope

The data of Sr–Nd isotope for the granitoids are listed in Table 5 and illustrated in Fig. 5b. The whole-rock Sr–Nd isotope characteristics of all the granitoids are comparable, indicating a similar source.

Initial  $^{87}\text{Sr}/^{86}\text{Sr}$  ratios and  $\epsilon_{\text{Nd}}(t)$  values of the K-feldspar granites were calculated using an age of 1178 Ma. Their initial  $^{87}\text{Sr}/^{86}\text{Sr}$  ratios are between 0.7162 and 0.7217, and the age-corrected  $\epsilon_{\text{Nd}}(t)$  values vary from  $-9.17$  to  $-9.24$ , corresponding to  $T_{\text{DM2}}$  ages of  $2523 \sim 2529$  Ma.

Initial  $^{87}\text{Sr}/^{86}\text{Sr}$  ratios and  $\epsilon_{\text{Nd}}(t)$  values of the biotite monzogranites were calculated using an age of 1105 Ma. Their initial  $^{87}\text{Sr}/^{86}\text{Sr}$  ratios are between 0.7246 and 0.7305, and the age-corrected  $\epsilon_{\text{Nd}}(t)$  values vary from  $-8.67$  to  $-9.98$ , corresponding to  $T_{\text{DM2}}$  ages of  $2424 \sim 2529$  Ma.

## Discussion

### Petrogenetic type: S-type, I-type, or A-type?

All the granitoids in the Solwezi Dome have high initial  $^{87}\text{Sr}/^{86}\text{Sr}$  ratios and negative  $\epsilon_{\text{Nd}}(t)$  values, distinguishing them from those of M-type granite. Furthermore, they are metaluminous to weak peraluminous, contain no aluminum-rich minerals (garnet or cordierite) and have low CIPW normative corundum ( $0 \sim 0.74\%$  and  $0.51 \sim 1.50\%$ , respectively), in contrast to strongly peraluminous S-type granites formed by partial melting of metapelitic protolith (Fig. 5d) (Clemens 2003; Zhao et al. 2018). As a result, the granitoids in the Solwezi Dome should be I-type or A-type.

**Table 4** Whole-rock major (wt%) and trace (ppm) element contents of the late-Mesoproterozoic granitoids in the Solwezi Dome

Rock	Metamorphic K-feldspar granite							Metamorphic biotite monzogranite							ZS33	
	ZS44	ZS45	ZS46	ZS48	ZS49	ZS50	ZS51	ZS52	ZS26	ZS25	ZS27	ZS28	ZS29	ZS30	ZS31	ZS33
No	71.5	72.6	73.1	71.5	71.8	72.1	72.7	72.5	68.7	71.4	69.2	66.3	69.3	66.1	69.1	69.8
SiO <sub>2</sub>	13.4	13.6	13.5	14.4	14.4	13.6	13.4	13.5	14.6	13.5	14.5	15.2	14.5	14.5	14.4	14.11
Al <sub>2</sub> O <sub>3</sub>	0.6	1.17	1.42	0.87	1.44	1.82	1.14	1.3	0.79	1.09	1.42	1.88	1.56	1.43	1.97	2.13
Fe <sub>2</sub> O <sub>3</sub>	FeO	0.8	0.65	0.88	0.46	0.44	0.97	0.76	2.6	1.8	2.25	3.26	1.81	2.45	1.78	0.8
CaO	1.05	1.09	0.92	1.06	1.02	1.11	1.08	1.04	1.41	1.45	1.88	2.16	1.85	1.82	1.81	1.62
MgO	0.58	0.63	0.52	0.55	0.43	0.65	0.57	0.58	1.15	0.8	1.09	1.52	1	1.34	0.96	0.89
K <sub>2</sub> O	6.04	6.24	6.26	6.18	6.24	6.15	6.24	5.78	5.18	4.68	3.84	5	5.34	5.68	5.16	5.5
Na <sub>2</sub> O	4.6	2.78	2.59	3.12	2.93	2.8	2.68	2.67	3.18	2.68	3.06	3.44	2.99	3.17	2.89	2.9
TiO <sub>2</sub>	0.21	0.25	0.23	0.21	0.2	0.27	0.22	0.24	0.56	0.44	0.54	0.91	0.56	0.76	0.52	0.48
P <sub>2</sub> O <sub>5</sub>	0.093	0.083	0.082	0.085	0.066	0.085	0.078	0.11	0.23	0.27	0.33	0.32	0.28	0.36	0.32	0.23
MnO	0.013	0.014	0.012	0.013	0.011	0.017	0.015	0.014	0.029	0.028	0.049	0.033	0.05	0.022	0.028	0.015
灼失	0.75	0.92	0.75	0.98	1.03	0.91	0.95	1.0	0.7	1.17	0.78	0.81	0.84	0.82	0.8	0.81
Total	99.89	99.93	99.93	99.92	99.97	99.95	99.92	99.93	99.72	99.81	99.75	99.63	99.79	99.75	99.81	99.91
CLA	43.64	47.79	47.88	47.98	48.72	47.15	47.47	47.33	48.69	49.32	50.52	52.50	50.93	50.75	48.84	48.60
<i>CIPW normal</i>																
Q	20.5	29.3	30.7	25.7	27.6	27.8	29.6	29.4	22.4	31.6	27.5	23.7	26.8	20.6	24.7	25.9
A	37.3	37.5	38.7	38.8	38.3	38.7	38.2	38.7	36.4	32.7	29.7	24.8	31.6	34.1	35.7	32.6
P	36.1	29.2	26.6	31.9	30.3	29.4	28.2	27.8	33.8	29.3	34.6	40.1	34.1	35.3	32.8	34.5
Mg <sup>#</sup>	39	38	33	37	30	36	34	35	38	32	34	36	35	36	37	35
Cu	12.5	9.53	8.74	8.98	7.96	7.04	7.31	8.46	50	11.8	7.01	12.5	15	48.1	17.1	6.97
Pb	15.8	17.5	18.7	16	16.8	12.6	13.2	15.4	17.3	25.1	18	9.83	24.6	12	25.6	21.8
Zn	18.3	18.5	15.9	12.8	15.7	14.2	11.9	13.1	22.1	20.4	34.9	24	42.1	23.6	22	27.7
Cr	5.74	6.32	5.78	5.65	6.65	6.8	5.24	5.89	21.7	14.1	21.1	32.4	15.8	17	15.6	11.2
Ni	6.92	6.35	5.18	5.24	5.2	5.94	5.82	5.53	12.7	9.24	12.6	13.2	10.3	12.1	9.56	7.53
Co	5.55	3.49	3	2.8	2.56	3.2	2.96	3.15	10.6	5.14	6.83	10.1	6.74	13.9	6.82	5.02
Rb	184	213	216	235	201	237	225	224	253	220	188	206	206	225	250	210
Rock																231
The K-feldspar granite																
No	ZS44	ZS45	ZS46	ZS48	ZS49	ZS50	ZS51	ZS52	ZS26	ZS25	ZS27	ZS28	ZS29	ZS30	ZS31	ZS33
Cs	0.49	0.6	0.57	0.6	0.54	0.78	0.61	0.61	1.67	1.07	1.45	1.6	1.5	1.51	1.18	0.96
Sr	297	233	234	213	238	254	225	252	358	249	221	252	334	236	308	259
Ba	1480	1070	978	1000	1040	1000	946	998	1570	1040	722	637	1160	1090	1270	1140
V	22.3	31	28.8	25.6	25.8	32.6	27	30	55	40.3	44	71.3	50	60.1	47.8	42.8
Sc	12.3	10.3	10.2	9.4	9.64	10.2	9.94	10.1	10.6	12.7	14	18.2	15	16.7	14.6	13.6
Nb	7.72	9.28	8.12	8.12	8.95	9.42	8.36	8.83	17.6	22.8	29.1	45.9	32.1	45.8	28.8	25.3
Ta	0.5	0.54	0.46	0.51	0.57	0.52	0.48	0.51	0.9	0.8	1.02	1.48	1.26	1.84	1.44	1.05
Zr	187	195	180	173	178	208	188	199	464	271	403	546	378	468	391	301
Hf	6.3	6.73	6.23	5.9	6.23	7.18	6.55	6.86	14.3	8.7	12.5	16.7	12	14.4	11.8	9.6
Ga	16.2	18.6	17.8	19.1	18.8	19.1	18	18.2	24.6	20.6	23.7	27.5	22.6	25.3	21.7	21.1
U	1.75	4.19	2.21	2.53	2.34	4.13	2.49	2.71	3.83	3.56	6.04	5.12	3.59	4.69	3.64	5.58
Th	21.8	53.4	42.4	45	40.7	54.7	38.9	49.1	103	57	76.8	83.1	56.6	80.3	69	57.8

**Table 4** (continued)

	La	69.2	56.4	68	85.1	50	66.2	149	80.7	112	146	95.7	112	119	102	101	130
Ce	60.3	145	110	130	108	175	99.8	132	310	156	191	281	195	216	225	205	221
Pr	8.45	17.2	13.9	16.5	14	20.7	12.8	16.2	33.6	19.8	27.5	34.9	22.5	27.3	26.6	23.1	26
Nd	30.9	61.1	49.8	57.5	49.3	72.3	45.4	56.8	118	71	97.2	121	78	97.3	93.4	80.5	93.5
Sm	5.24	10.2	8.12	9.24	7.92	11.8	7.68	9.27	16.5	11.2	15.4	17.6	10.9	14.5	13.1	11.3	15.4
Eu	1.54	1.63	1.44	1.5	1.44	1.74	1.33	1.51	2.4	1.63	1.73	1.82	1.78	1.92	1.9	1.81	1.94
Gd	7.15	11.7	9.76	11.2	9.47	13.4	8.76	10.2	18.7	13.9	18.5	22.1	14	17.6	16.8	13.2	18
Tb	0.66	1.2	0.95	1.08	0.91	1.34	0.89	1.07	2.02	1.52	2.2	2.33	1.35	2	1.67	1.39	1.91
Dy	1.86	3.63	2.77	3.21	2.73	3.94	2.83	3.47	7.89	6.34	9.79	9.01	5.11	9.08	6.43	5.67	6.6
Ho	0.3	0.55	0.42	0.51	0.42	0.6	0.42	0.52	1.34	1.18	1.79	1.69	1.01	1.76	1.2	1.11	1.39
Er	1.16	2	1.52	1.91	1.51	2.14	1.47	1.8	4.1	3.92	5.7	5.65	3.65	5.76	4.24	3.98	3.84
Tm	0.11	0.17	0.14	0.18	0.13	0.18	0.14	0.16	0.42	0.46	0.67	0.62	0.46	0.72	0.48	0.5	0.43
Yb	0.8	1.24	0.96	1.28	0.95	1.29	1	1.19	2.67	2.82	3.86	3.83	2.87	4.2	2.86	3.14	2.92
Rock	The biotite monzogranite																
No	ZS44	ZS45	ZS46	ZS48	ZS49	ZS50	ZS51	ZS52	ZS25	ZS26	ZS27	ZS28	ZS29	ZS30	ZS31	ZS32	ZS33
Lu	0.12	0.19	0.15	0.19	0.14	0.21	0.16	0.18	0.38	0.38	0.51	0.53	0.4	0.56	0.38	0.43	0.41
Y	6.43	12.7	10	12.3	9.8	13.8	9.7	12.4	31.3	29.4	45.4	42.1	25.7	44	30.6	29	26.5
Mg <sup>#</sup>	39	38	33	37	30	36	34	35	38	34	36	35	36	37	36	35	40
A/CNK	0.84	1.04	1.06	1.04	1.08	1.01	1.03	1.04	1.04	1.06	1.07	1.11	1.06	1.10	1.02	1.01	1.03
K <sub>2</sub> O/ Na <sub>2</sub> O	1.31	2.17	2.41	2.01	2.11	2.23	2.29	2.34	1.82	1.93	1.53	1.12	1.67	1.68	1.97	1.71	2.22
Sr/Y	46	18	23	17	24	18	23	20	11	8	5	6	13	5	10	12	10
Molar CIA=100×(Al <sub>2</sub> O <sub>3</sub> /Al <sub>2</sub> O <sub>3</sub> +CaO+K <sub>2</sub> O+N <sub>2</sub> O), Mg <sup>#</sup> =Mg <sup>2+</sup> /(Mg <sup>2+</sup> +Fe <sup>2+</sup> )×100																	

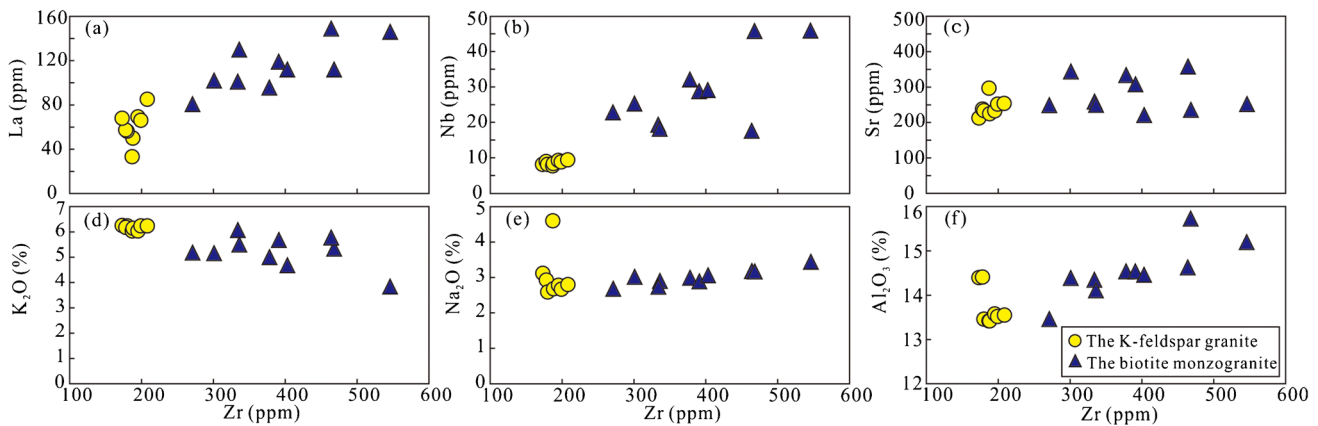
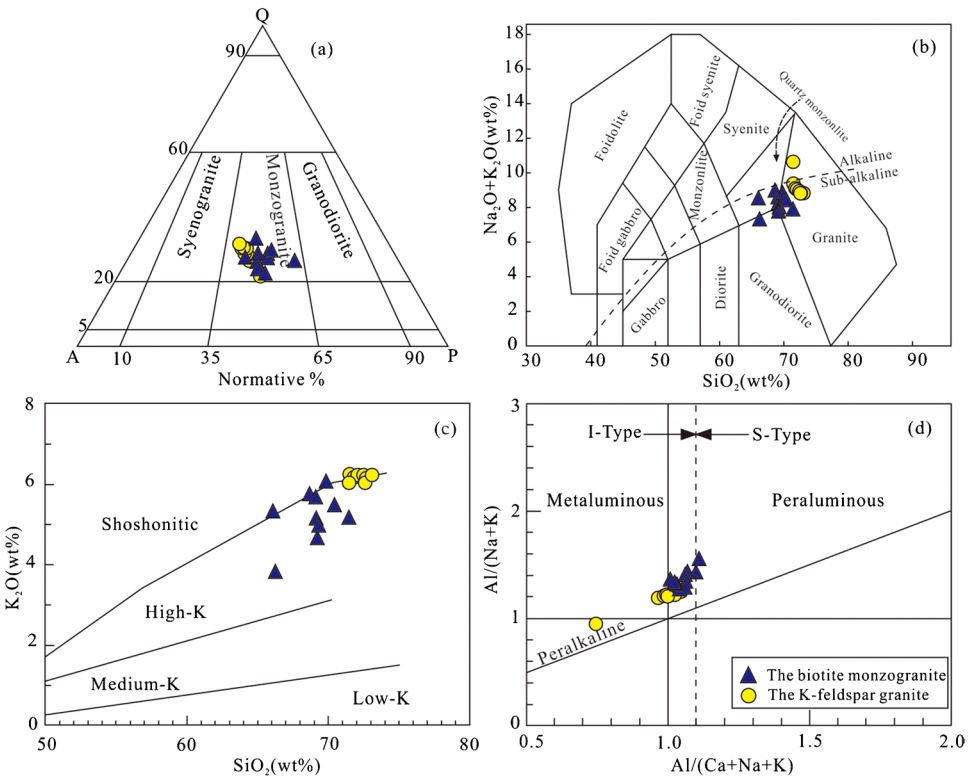


**Fig. 6** Plot of Zr vs (a) La, (b) Nb, (c) Sr, (d)  $K_2O$ , (e)  $Na_2O$  and (f)  $Al_2O_3$  for the granitoids in the Solwezi Dome

**Fig. 7** (a) Q–A–P plot (Streckeisen 1976); (b) ( $K_2O + Na_2O$ ) vs.  $SiO_2$  (Middlemost 1994); (c)  $K_2O$  vs.  $SiO_2$  (Roberts & Clemens 1993); (d) A/NK vs. A/CNK (Maniar & Piccoli 1989) diagrams for the granitoids in the Solwezi Domes



### The K-feldspar granite

The A/CNK values ( $0.84 \sim 1.08$ ) and  $P_2O_5$  contents ( $0.07 \sim 0.11$  ppm) of the K-feldspar granites are low, and there is an increase in Y and Th as Rb increases (Fig. 9n, o), which are typical characteristics of I-type granite (Maniar & Piccoli 1989; Li et al. 2007; Liu et al. 2009). The calculated zircon saturation temperatures ( $T_{zr}$ ) for the K-feldspar granites using the equation of Watson & Harrison (1983) are  $771 \sim 806^\circ C$ , which are similar to the formation temperature of I-type granite ( $781^\circ C$ , King et al. 1997)

(Fig. 10). Meanwhile, all of the samples fall in the transition field between fractionated and unfractionated I-, S-, and M-type granite on the petrogenetic discrimination diagrams (Fig. 11). Therefore, we believe that the K-feldspar granites are I-type.

### The biotite monzogranite

The biotite monzogranites have relatively low Nb ( $17.6 \sim 45.9$  ppm), Ce ( $156 \sim 310$  ppm), Zr ( $271 \sim 546$  ppm), Y ( $25.7 \sim 45.4$  ppm),  $Zr + Nb + Ce + Y$  ( $479 \sim 823$  ppm), and  $10,000 \times Ga/Al$  ratios ( $2.85 \sim 3.42$ ), which are similar

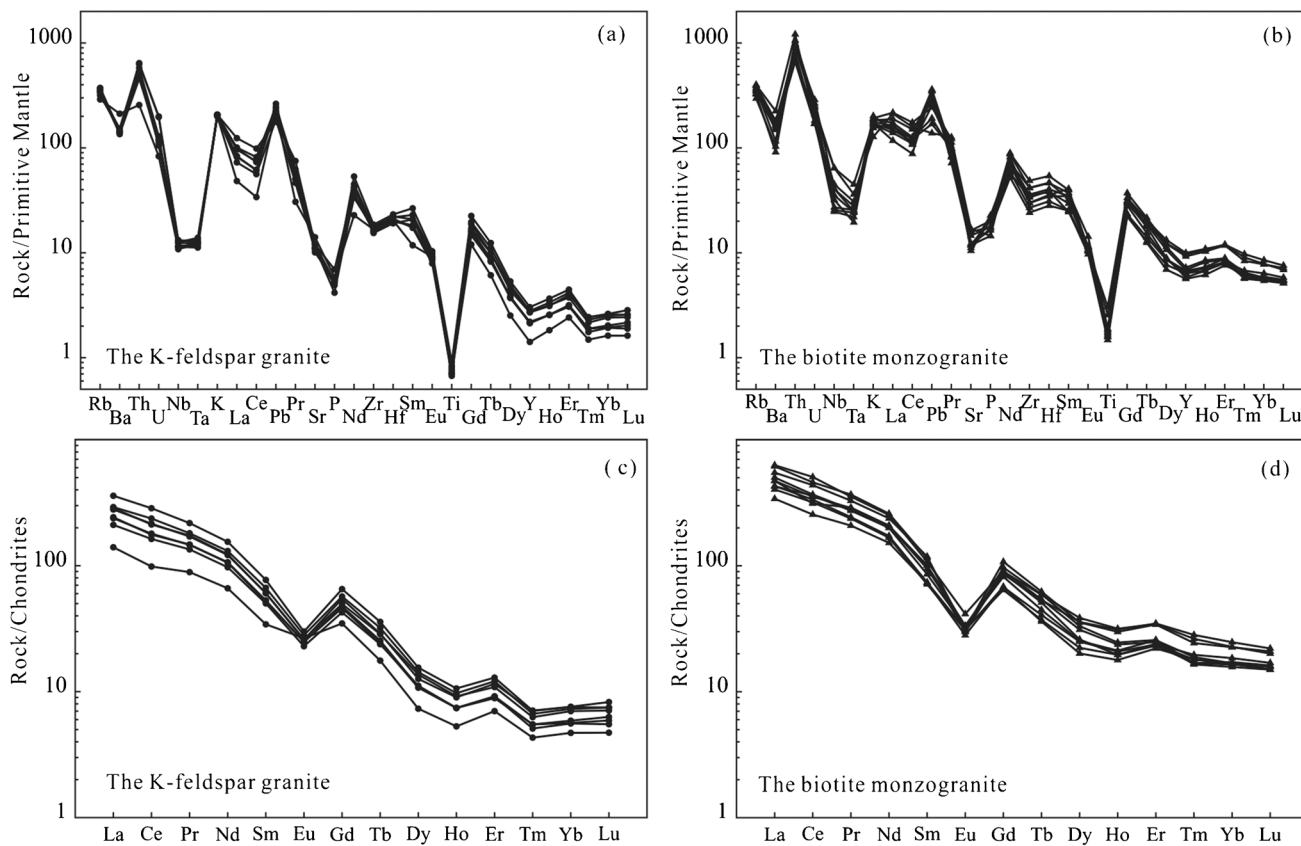


**Fig. 8** Chondrite-normalized REE patterns and Primitive Mantle (PM) normalized trace element diagrams for the K-feldspar granites (**a, c**) and the biotite monzogranites (**b, d**) in the Solwezi Dome. The values of chondrite and PM are from Sun & McDonough (1989)

to the geochemical characteristics of A-type granite (Whalen et al. 1987; Collins et al. 1982). Their  $T_{zr}$  are 836~902°C (Fig. 10), which are obviously higher than I- and S-type granite but similar to A-type granite (839°C, King et al. 1997). All the samples fall in the A-type granite field (Fig. 11). Therefore, we believe that the biotite monzogranites are A-type.

## Petrogenesis

### The K-feldspar granite

The K-feldspar granites have high initial  $^{87}\text{Sr}/^{86}\text{Sr}$  values (0.7162~0.7217), negative whole-rock  $\epsilon_{\text{Nd}}(t)$  values ( $-9.17 \sim -9.24$ ) and zircon  $\epsilon_{\text{Hf}}(t)$  values ( $-12.03 \sim -7.10$ ), corresponding to  $T_{\text{DM2}}$  ages of 2523~2529 Ma and 2423~2728 Ma, respectively, implying that the granitic magma was primarily derived from anatexis or remelting of Neoarchean crust (Allègre & Othman 1980). The  $\text{Mg}^{\#}$  is a useful index of discriminating melts of purely crustal origin from those that have interacted with mantle-derived magma. Melts from the basaltic lower continental crust are characterized by low  $\text{Mg}^{\#}$  values ( $< 40$ ) regardless of the degree of

melting, whereas those with higher  $\text{Mg}^{\#}$  values ( $> 40$ ) can only be generated by involvement with a mantle component (Rapp & Watson 1995; Liu et al. 2014). The  $\text{Mg}^{\#}$  values of the K-feldspar granites are 30~39, which fall in the crustal melts and the lower crustal melts (TTG) fields but deviate from the pure crustal partial melts on the  $\text{SiO}_2-\text{Mg}^{\#}$  diagram (Fig. 12), implying that the magma might be primarily crustal-derived with a tiny component of mantle-derived magma. The zircon  $\epsilon_{\text{Hf}}(t)$  values are heterogeneous (up to 4.93 units), further implying a hybrid source of mixing between crust-melts and mantle-melts (Chiu et al. 2009). A large number of Neoarchean detrital zircons (2710~2460 Ma) (Liu et al. 2019; Master et al. 2005) and a suite of metamorphic and igneous rocks (2560~2540 Ma) (Key et al. 2001) have been identified in the Lufilian Arc, implying that Neoarchean was an important period of crustal accretion in this belt. Combined with the Neoarchean  $T_{\text{DM2}}$  ages; we can further suggest that the K-feldspar granites might be derived from partial melting of Neoarchean basement. Such a genetic relationship between K-rich granite and TTG protolith has also been widely documented in many Archean cratons (Mark 1999; Shang et al. 2007; Zhao et al. 2008). In addition, the K-feldspar granites have strongly fractionated

**Table 5** Whole-rock Rb–Sr and Sm–Nd isotopic composition of the late-Mesoproterozoic granitoids in the Solwezi Dome

Sample	Age (Ma)	Rb (ppm)	Sr (ppm)	Sm (ppm)	Nd (ppm)	$^{87}\text{Rb}/^{86}\text{Sr}$	$^{87}\text{Sr}/^{86}\text{Sr}$	$(^{87}\text{Sr}/^{86}\text{Sr})_i$	$^{147}\text{Sm}/^{144}\text{Nd}$	$^{143}\text{Nd}/^{144}\text{Nd}$	$(^{143}\text{Nd}/^{144}\text{Nd})_i$	$\varepsilon_{\text{Nd}(t)}$	$T_{\text{DM1}}$	$T_{\text{DM2}}$
ZS44	1178	184	297	5.24	30.9	1.7930	0.746448	0.716204	0.1025	0.511437	0.510644453	-9.24	2340	2529
ZS45	1178	213	233	10.2	61.1	2.6457	0.766319	0.721691	0.1009	0.511428	0.510647834	-9.17	2319	2523
ZS25	1105	253	358	16.5	118	2.0453	0.756918	0.724572	0.0845	0.511381	0.510768134	-8.67	2082	2424
ZS26	1105	220	249	11.2	71	2.5570	0.769421	0.728982	0.0953	0.511402	0.510710187	-9.80	2245	2515
ZS28	1105	206	252	17.6	121	2.3658	0.767893	0.750478	0.0879	0.511370	0.510732103	-9.37	2151	2481
ZS33	1105	210	259	15.4	93.5	2.3466	0.763154	0.726043	0.0995	0.511423	0.510701006	-9.98	2299	2529

LREE patterns [ $(\text{La}/\text{Sm})_N = 3.99 \sim 4.63$ ] and HREE patterns [ $(\text{Gd}/\text{Yb})_N = 6.92 \sim 8.38$ ], as well as medium negative Eu anomalies ( $\delta\text{Eu} = 0.42 \sim 0.77$ ) (Fig. 8a) and obviously depleted in Sr (Fig. 8b), but their Sr/Y ratios are high (17.32~46.19), implying that the source melting occurred at pressures between the garnet and plagioclase stability field, corresponding to a slightly thickened crust of 0.8~1.4 Gpa (Zhang et al. 2011; Zhao et al. 2018).

The contents of MgO, FeO<sub>t</sub>, TiO<sub>2</sub>, Al<sub>2</sub>O<sub>3</sub>, Ni, V, Rb, and Zr stay essentially constant as SiO<sub>2</sub> increases (Fig. 9), indicating a low-degree fractional crystallization of the K-feldspar granite; this result is compatible with Fig. 11. Rb/Sr and Sr, Ba and Sr, Dy and Er,  $(\text{La}/\text{Yb})_N$ , and La suggest that the magma underwent low-degree fractional crystallization of plagioclase, K-feldspar, amphibole, and some accessory minerals (e.g., monazite, epidote) (Fig. 13). Meanwhile, the depletion of Nb–Ta–Ti and P might be related to the fractionation of the Ti-bearing phases (e.g., ilmenite and titanite) and apatite, respectively. In summary, we can speculate that the K-feldspar granites were most likely formed by partial melting of Neoarchean basement in a slightly thickened lower crust, followed by low-degree fractional crystallization of plagioclase, K-feldspar, amphibole, and some accessory minerals.

### The biotite monzogranite

The biotite monzogranites have high initial  $^{87}\text{Sr}/^{86}\text{Sr}$  values (0.7246~0.7305), negative whole-rock  $\varepsilon_{\text{Nd}}(t)$  values ( $-8.67 \sim -9.98$ ) and zircon  $\varepsilon_{\text{Hf}}(t)$  values ( $-14.85 \sim -9.35$ ), corresponding to  $T_{\text{DM2}}$  ages of 2424~2529 Ma and 2511~2847 Ma, respectively, implying that the magma was also derived from partial melting of Neoarchean crust. Melting experiments demonstrate that dehydration melting of fluid-bearing tonalitic and granodioritic rocks can generate A-type granitic melts (Skjerlie & Johnston. 1993; Patiño Douce 1997). The biotite monzogranites and the K-feldspar granites have similar geochemical components; both of them are within or close to the experimentally produced melts of crustal origin (Fig. 9a–i), indicating that the magma probably also derived from partial melting of Neoarchean basement. The Mg<sup>#</sup> values are 33~40, which fall in the crustal melts and the lower crustal melts (TTG) fields; however, they also have a clear evolution trend to the mantle-melts (Fig. 12). Combined with the higher MgO, TiO<sub>2</sub>, Cr, Ni, and the heterogeneous zircon  $\varepsilon_{\text{Hf}}(t)$  values (up to 5.50 units), we speculate that some mantle melts might be involved during the crustal-dominated melting process. Meanwhile, the strongly fractionated LREE patterns [ $(\text{La}/\text{Sm})_N = 3.99 \sim 4.63$ ] and relatively flat HREE patterns [ $(\text{Gd}/\text{Yb})_N = 3.38 \sim 5.76$ ], obviously negative Eu anomalies ( $\delta\text{Eu} = 0.28 \sim 0.45$ ) (Fig. 8c), depleted in Sr and lower Sr/Y ratios (4.87~13.0), implying that the source might be at relatively shallow depths where plagioclase was present and

garnet was absent, corresponding to the middle-lower crust of 0.8~1.0 Gpa (Patiño Douce & Beard 1995; Watkins et al. 2007; Zhao et al. 2008; Sarjoughian et al. 2016).

The biotite monzogranites display a higher degree fractional crystallization of plagioclase, K-feldspar, amphibole, apatite, titanite, and some accessory minerals than the K-feldspar granites (Fig. 13). In summary, the biotite monzogranites were also likely formed by partial melting of Neoarchean basement, but at relatively shallow depths with a minor quantity of mantle melts, followed by fractional crystallization of plagioclase, K-feldspar, amphibole, and some accessory minerals.

## Tectonic setting and implications

### Tectonic setting

Granitoid types were potentially proposed to be related to tectonic setting. A granitoid can well be used as a geodynamic indicator when it is correctly classified and also precisely dated (Pearce et al. 1984; Foerster et al. 1997; Barbarin 1999; Dong et al. 2011). It has been demonstrated that the granitoids formed in various tectonic settings usually have different geochemical features, which can be used to infer the formation environment (Pearce et al., 1984).

Previous researches have revealed that continental collision is an important factor that contributes to crustal thickening in the orogenic belt (Zhang et al. 2006; Wu et al. 2005). The petrogenetic analysis mentioned above reveals that the K-feldspar granites were the products of partial melting of the slightly thickened lower crust; therefore, they were most likely generated in a syn-collisional environment. On the tectonic discrimination diagrams of Rb-(Y+Nb), Nb-Y, Nb-SiO<sub>2</sub>, and R1-R2, the K-feldspar granites fall in the field of the syn-collisional granites (Fig. 14), further suggesting that they were generated in a syn-collisional environment.

A-type granite is usually associated with extensional tectonic setting (Bonin 2007; Karsli et al. 2012; Martin et al. 1994; Zhao et al. 2008). The biotite monzogranites have characteristics of A-type granites, and they mainly fall in the fields of the post-collisional or the within-plate granites (Fig. 14), combined with the geochronological data and tectonic environment of the K-feldspar granite; we believe that the biotite monzogranites were likely generated in a post-collisional environment.

### The provenance of detrital material

A substantial quantity of Mesoproterozoic detrital zircons were found in different areas of the Lufilian Arc, such as in the Chambishi Basin (1.50~1.05 Ga, Liu et al. 2019), Konkola and Kipushi (1231~1025 Ma, Master et al.

2005), Solwezi (1220~931 Ma, Xu et al. 2021), and Likasi (1.1~1.6 Ga, Rainaud et al. 2003). The U-Pb ages of the granitoids in the Solwezi Dome are between 1178±15 and 1105±7 Ma, which are consistent with the age peak of detrital zircons in the garnet mica schist near Solwezi (Xu et al. 2021), implying that the late-Mesoproterozoic granitoids were important sources for detrital materials of the Katanga Supergroup.

### Buried Mesoproterozoic orogen in the Lufilian Arc

Tectonic discrimination diagrams and geochronological data show that the Mesoproterozoic granitoids in the Solwezi Dome are related with orogeny (Fig. 14). As we know, the Mesoproterozoic orogenies developed in Central Africa are the Kibaran event (1.42~1.0 Ga, Kokonyangi et al. 2004; Debruyne et al. 2015; Tack et al. 2010) and the Irumide event (1.05~0.95 Ma, De Waele et al. 2006, 2009). In the Irumide Belt, voluminous syn- to post-kinematic Irumide granitoids emplaced between 1.05 and 0.95 Ga, peak metamorphism is diachronous across the belt and bracketed between 1.05 Ga in the southeast and 1.02 Ga in the northwest. The zircon U-Pb ages of the Solwezi granitoids are 1178±15 Ma~1105±7 Ma, which are obviously earlier than the emplaced ages of the Irumide granitoids, and the tectonic environment of syn- to post-collision is also inconsistent with the tectonic evolution stage of the Irumide Belt. Therefore, we speculate that the granitoids may be related to the Kibaran orogeny.

The explanation for the *ca.* 400 Ma magmatic and metamorphic history of the Kibaran Belt remains enigmatic (Tack et al. 2010; Debruyne et al. 2015). In the southern part of this belt, Kampunzu et al. (1998) consider that the Kibaran deformation events mark the development of an active continental collision (*ca.* 1.4~1.25 Ga), followed by a continental collision (*ca.* 1.25~1.0 Ga), but there is no consensus on this interpretation (Klerkx et al. 1987). The latest research on the arc-type signature of the mafic intrusions (Kokonyangi et al. 2006) and the depositional or erosional hiatus (Fernandez-Alonso et al. 2012) indicate the proposed transition from accretionary tectonics and sedimentation toward a collisional setting during *ca.* 1420~1375 Ma (Debruyne et al. 2015); the following medium-pressure and medium-temperature metamorphism at 1079±14 Ma (Kokonyangi et al. 2001) is mainly a far-field tectonic linkage between the Kibaran Belt and the Irumide Belt (Johnson et al. 2005).

Geological constraints on the margins of the Congo-Tanzania-Bangweulu lack evidence for collisional orogenesis at the late stage of the Kibaran orogeny; however, in the southern part of Africa, a substantial quantity of late-Mesoproterozoic magmatism has been identified, and one possible interpretation is that they are related to a buried

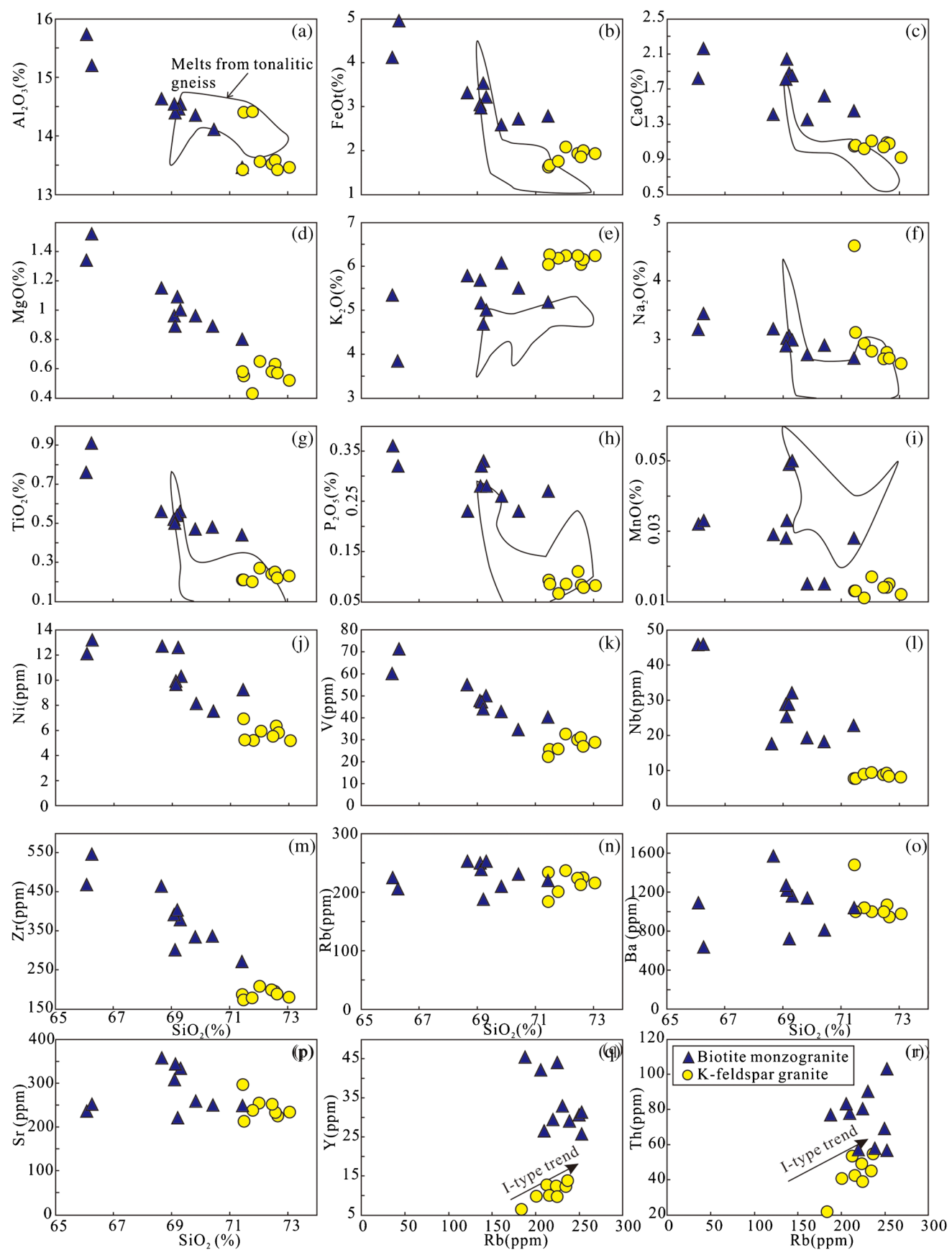


**Fig. 9** Harker plots of major and selected trace elements of the granitoids in the Solwezi Dome. Solid line range is the experimentally produced melts of crustal origin (Skjerlie & Johnston 1993)

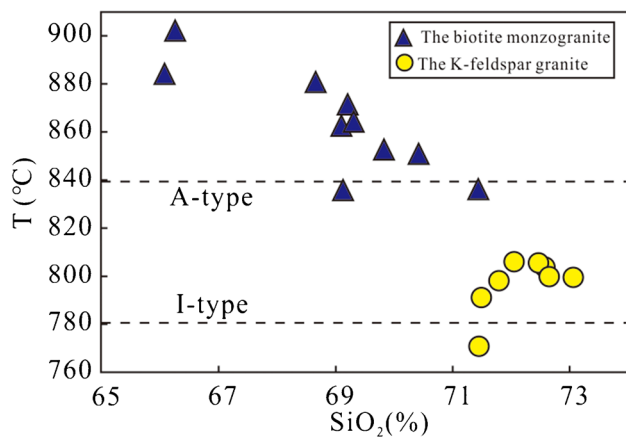


**Fig. 10** SiO<sub>2</sub> vs. the calculated zircon saturation temperature for the granitoids in the Solwezi Dome. The calculated zircon saturation temperatures are after Watson & Harrison (1983), the temperatures of I- and A-type granite are from King et al. (1997)

southwestern continuation of the Kibaran Belt (Singletary et al. 2003; Bulambo et al. 2004). In the Choma-Kalomo Block, ages of the two main magmatic pulses have recently been confirmed by SHRIMP dating of zircon, which have yielded a crystallization age of  $1368 \pm 10$  Ma (Singletary et al. 2003) for the syn-tectonic granitoid and ages between  $1188 \pm 11$  and  $1174 \pm 27$  Ma (Bulambo et al. 2004) for the post-tectonic granites (Hanson et al. 1988). Hanson et al. (1988) argued that the Choma-Kalomo Block represents part of a larger Mesoproterozoic orogen that continues in the subsurface into Botswana to the southwest along strike. Bulambo et al. (2004) described that the Choma-Kalomo Block may have been detached from the Kibaran Belt during a rift-drift stage of the Katangan basin. In the Ghanzi-Chobe Belt, U-Pb geochronological data constrain granitoid plutonism and amphibolite-facies ductile deformation to have occurred between  $1.20 \sim 1.15$  and  $1.1$  Ga (crystallization age of post-tectonic intrusion) (Singletary et al. 2003). In the Namaqua Belt exposed still farther southwest along strike, the rocks record ductile deformation, regional metamorphism at variable grades, and pre- to synorogenic magmatism at  $1.38$  to  $1.20$  Ga (Cornell et al. 1992; Hoal & Heaman 1995; Robb et al. 1999; Gutzmer et al. 2000). Singletary

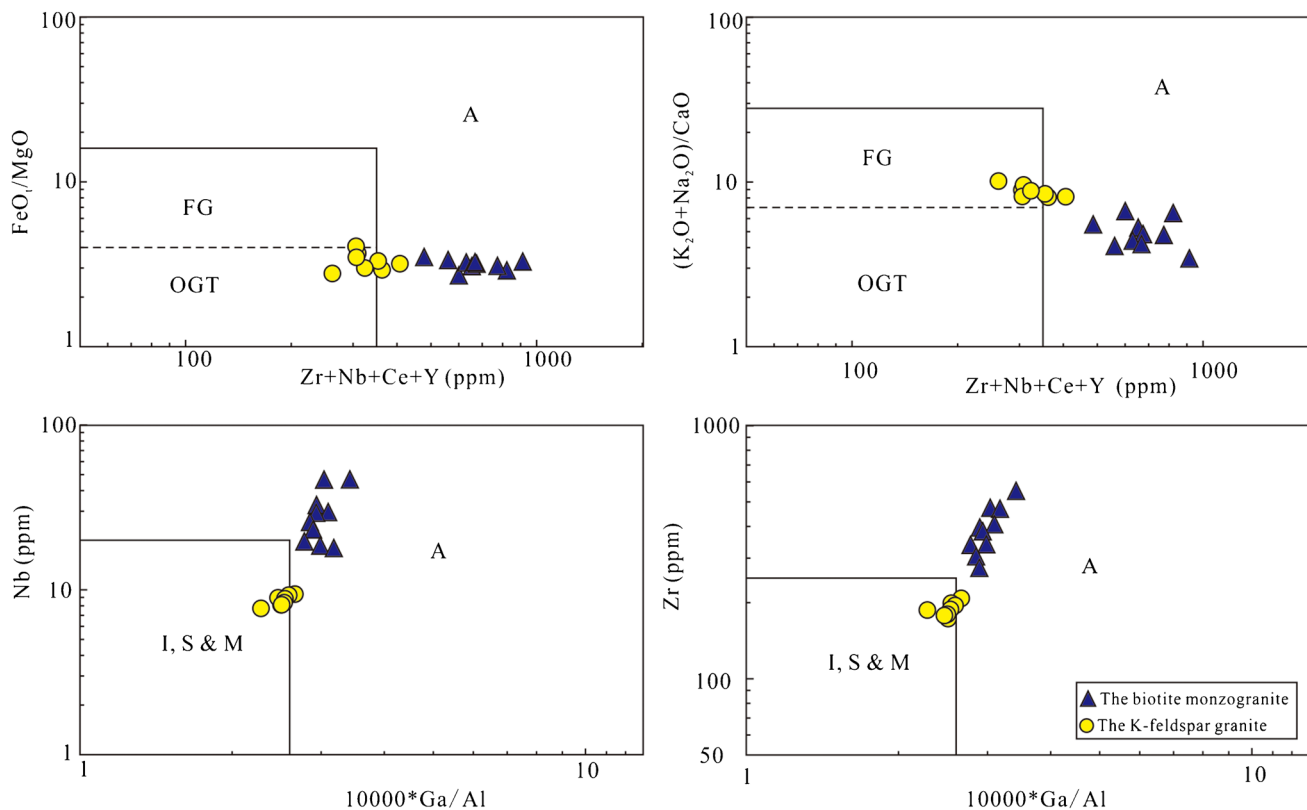


**Fig. 11** FeO<sub>t</sub> vs. (Zr+Nb+Ce+Y) (a), (K<sub>2</sub>O+Na<sub>2</sub>O)/CaO vs. (Zr+Nb+Ce+Y) (b), Nb vs. 10,000\*Ga/Al (c), and Zr vs. 10,000\*Ga/Al (d) discrimination diagrams of Whalen et al. (1987),

showing that the K-feldspar granites are I-type whereas the biotite monzogranite are A-type. FG: Fractionated felsic granites; OGT: unfractionated I-, S-, and M-type granites

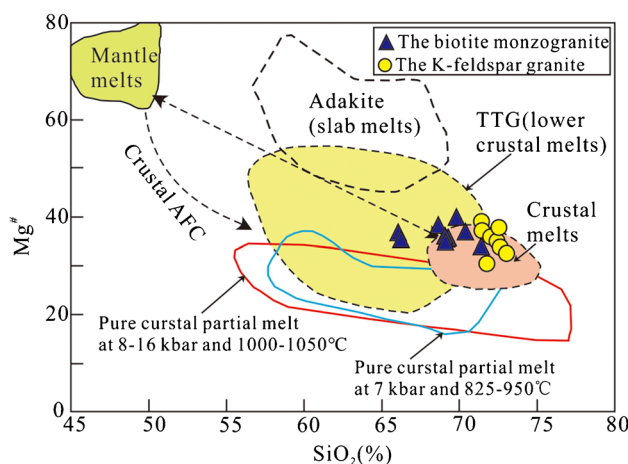
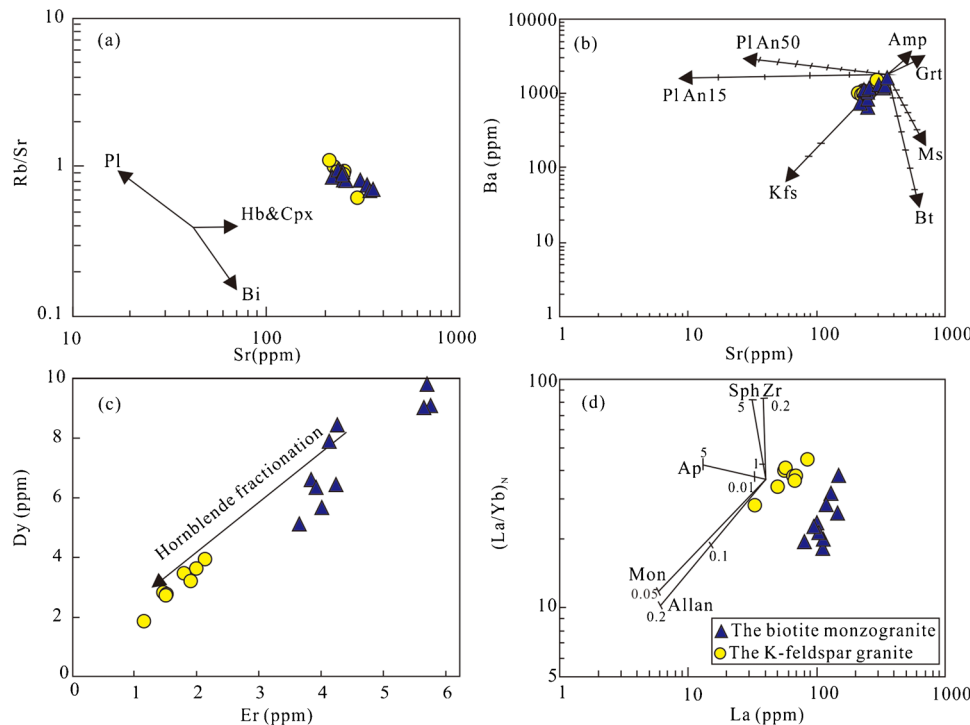


**Fig. 12** Mg<sup>#</sup> vs. SiO<sub>2</sub> diagram suggesting that the parental magma sources of the granitoids in the Solwezi Dome are not pure crustal partial melts but are mainly derived from crustal-melts (Dokuz 2011) and mixed with a small amount of mantle-melts (Kinzler, 1977). Data sources: the fields of pure crustal partial melts determined in experimental studies on the dehydration melting of low-K basaltic rocks at 8~16 kbar and 1000~1050 °C and medium- to high-K basaltic rocks at 7 kbar and 825~950 °C are from Rapp & Watson (1995) and Sisson et al. (2005), respectively. The crustal AFC is from Stern & Kilian (1996), and the TTG (lower-crustal melts) and adakite (slab melts) are taken from Condie (2005)

et al. (2003) inferred that the Choma-Kalomo Block, coeval parts of the Ghanzi-Chobe Belt, and the Namaqua Belt belong to a single, northeast-trending Mesoproterozoic orogen.

**Fig. 13** Magma evolution discrimination diagrams for the granitoids in the Solwezi Dome. Rb/Sr vs. Sr (a), Ba vs. Sr (b), Dy vs. Er (c), and (La/Yb)<sub>N</sub> vs. La (d) showing the trending of fractional crystallization



Because of thick Neoproterozoic and younger cover, it is impossible to directly trace this Mesoproterozoic orogen farther to the southwest (Key & Mapeo 1999). However, the K-feldspar granite, which is not only consistent with the contemporaneous granites in the Choma-Kalomo Block, the Ghanzi-Chobe Belt, and the Namaqua Belt in terms of petrogenesis and tectonic environment, but also allows these belts to be geographically connected to the Kibaran Belt, thus further proving that there is a buried southwestern continuation of the Kibaran Belt.

#### Extension-related magmatism in the Lufilian Arc

Bimodal volcanism is generally considered to be the dominant igneous assemblages in the continental rift zone (Tacket et al., 2010; Kampunzu et al., 1998). A substantial quantity of late-Mesoproterozoic mafic and felsic volcanic rocks and small granitic intrusions have been identified in the buried Kibaran Belt (Singletary et al. 2003).

In the Ghanzi-Chobe Belt, all dated rhyolites have a U-Pb zircon age of 1106±2 Ma (Schwartz et al. 1996); the related dolerite sills have yielded a conventional U-Pb zircon age of 1105±2 Ma (Hanson et al. 1998) and a SHRIMP zircon and baddeleyite age of 1099±9 Ma (Wingate 2001). In the Damara belt, rhyolites within bimodal assemblages have a U-Pb zircon age of 1094±20 Ma (Hegenberger & Burger 1985). Still farther southwest, metarhyolite has a U-Pb zircon age of 1107±2 Ma (Pfurr et al. 1991). In addition, the Munali Hill Granite (*ca.* 1090 Ma) and the Mpande Gneiss (*ca.* 1100 Ma) in the Zambezi Belt, which are considered to

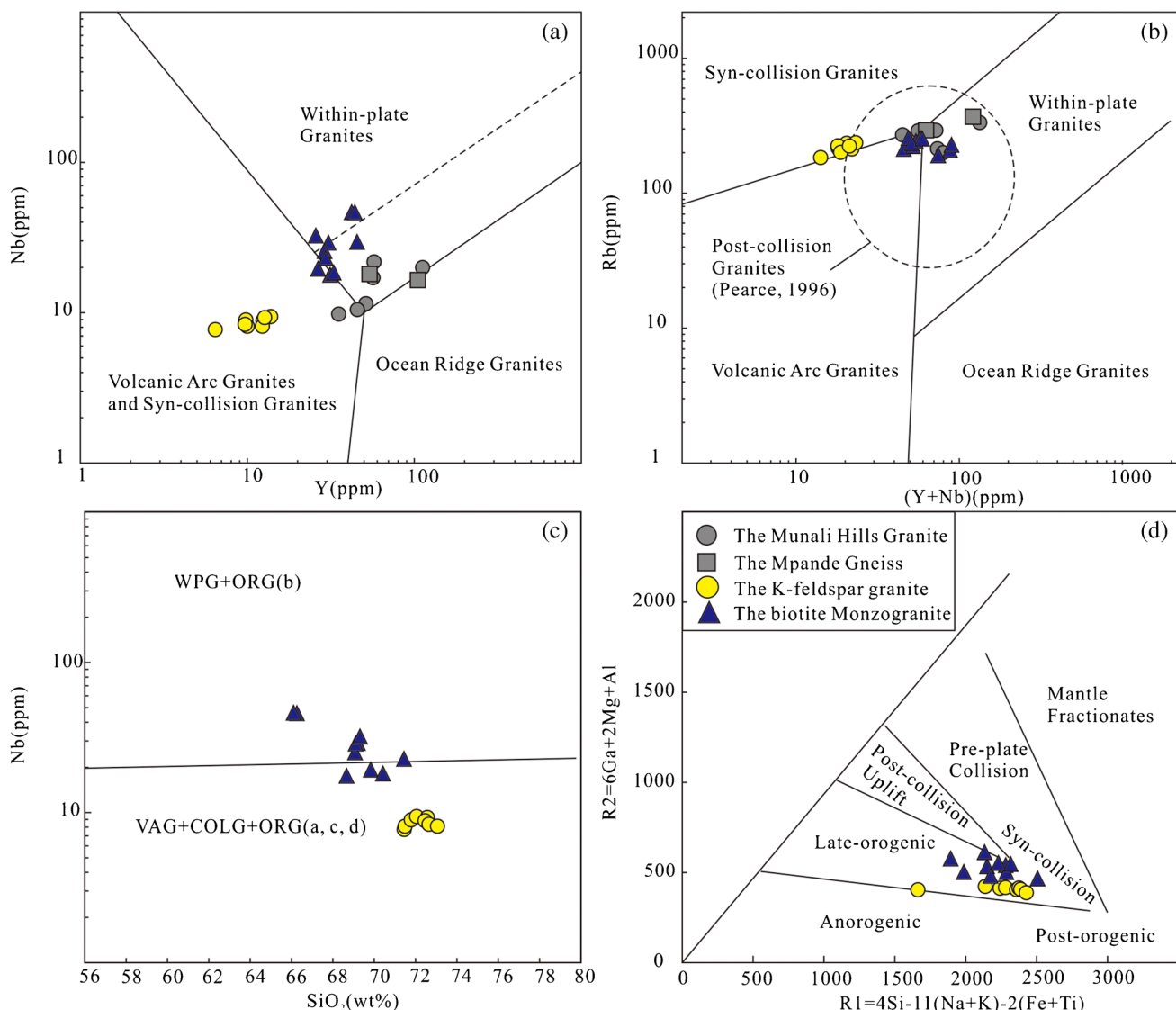


**Fig. 14** Tectonic discrimination diagrams of the granitoids in the Solwezi Dome. (a) Nb versus Y, (b) Rb versus  $(Y + Nb)$  and (c) Nb versus  $\text{SiO}_2$  (Pearce et al. 1984), (d) R1-R2 diagram of Batchelor &

Bowden (1985). Data source: the data of the Munali Hill Granite and the Mpande Gneiss are from Katongo et al. (2004)

be related to the Irumide orogeny (Katongo et al. 2004), are also mainly in the field of the within-plate granites (Fig. 12).

All these rocks appear to represent a single episode of rift-related magmatism. Based on the studies of magmatism in the Ghanzi-Chobe Belt, which have geochemical signatures of post-orogenic, within-plate rhyolites, Kampunzu et al. (1998) pointed out that superimposition of the rift on an older Mesoproterozoic orogen suggests that rifting and bimodal magmatism were triggered by extensional collapse of previously thickened crust. Although rift-related basic magmatism have not been found in the Lufilian Arc, the geochronology, petrogenesis, and tectonic environment of the biotite monzogranite are consistent with the magmatism mentioned above; therefore, it can be inferred that the

Lufilian Arc was also in a extensional environment of post-collision at ca. 1.10 Ga.

## Conclusions

Based on the field investigations, geochemical analyses and Sr–Nd–Hf isotopic studies of the late-Mesoproterozoic granitoids in the Solwezi Dome, the following conclusions are drawn:

- The Solwezi Dome complex is composed of the gneissic K-feldspar granite and the gneissic biotite monzogranite; LA-MC-ICP-MS zircon dating results

- show that the crystallization ages of the K-feldspar granites and the biotite monzogranites were  $1178 \pm 15$  Ma and  $1109 \pm 7$  Ma~ $\sim 1105 \pm 7$  Ma, respectively, suggesting that they are late-Mesoproterozoic magmatism.
- (2) The petrological and geochemical data show that the K-feldspar granites are I-type, which formed by partial melting of Neoarchean basement in a slightly thickened lower crust; the biotite monzogranites are A-type, which also formed by partial melting of Neoarchean basement but at a relatively shallow depths.
  - (3) The Lufilian Arc, the Zambezi Belt, the Choma-Kalomo Block, and the Ghanzi-Chobe Belt, and so on, may represent a buried southwestern continuation of the Kibaran Belt. The late-Mesoproterozoic granitoids in the Lufilian Arc are probably related to the Kibaran orogeny, which are the productions of syn-collisional and post-collisional stages, respectively.

**Acknowledgements** Sincere thanks are extended to the editor and anonymous reviewers, whose valuable comments were particularly helpful. We also thank Li-bo Zuo, Wen-gang Wang, and Jia-run Tu for helping with the Sr-Nd analysis, U-Pb dating, and Lu-Hf analysis. In addition, Chipilauka Mukofu, Alphet Phaskani Dokowe, and Ezekiah Chikambwe from the Geological Survey Department of Zambia, who provided sampling and coordination during the implementation of the project, are also thanked here.

**Funding** This study was financially supported by the Evaluation of Large Copper and Cobalt Resource Bases in Central Africa (No: DD20190439), Geological Survey Project of Southern Africa (No. DD20221801).

## Declarations

**Conflict of interest** The authors declare no competing interests.

## References

- Allègre CJ, Othman DB (1980) Nd-Sr isotopic relationship in granitoid rocks and continental crust development: a chemical approach to orogenesis. *Nature* 286(5771):335–342
- Armstrong RA, Master S, Robb LJ (2005) Geochronology of the Nchanga granite, and constraints on the maximum age of the Katanga Supergroup, Zambian Copperbelt. *J Afr Earth Sc* 42(1–5):32–40
- Barbarin B (1999) A review of the relationships between granitoid types, their origins and their geodynamic environments. *Lithos* 46:605–626
- Batchelor RA, Bowden P (1985) Petrogenetic interpretation of granitoid rock series using multicationic parameters. *Chem Geol* 48(1–4):43–55
- Batumike MJ, Kampunzu AB, Cailteux JH (2006) Petrology and geochemistry of the Neoproterozoic Nguba and Kundelungu Groups, Katangan Supergroup, southeast Congo: implications for provenance, paleoweathering and geotectonic setting. *J Afr Earth Sc* 44(1):97–115
- Batumike MJ, Cailteux JLH, Kampunzu AB (2007) Lithostratigraphy, basin development, base metal deposits, and regional correlations of the Neoproterozoic Nguba and Kundelungu rock successions, central African Copperbelt. *Gondwana Res* 11(3):432–447
- Blichert-Toft J, Albarède F (1997) The Lu-Hf isotope geochemistry of chondrites and the evolution of the mantle-crust system. *Earth Planet Sci Lett* 148(1–2):243–258. [https://doi.org/10.1016/S0012-821X\(97\)00040-X](https://doi.org/10.1016/S0012-821X(97)00040-X)
- Bonin B (2007) A-type granites and related rocks: evolution of a concept, problems and prospects. *Lithos* 97(1–2):1–2
- Bulambo M, De Waele B, Kampunzu AB, Tembo F (2004) SHRIMP U-Pb geochronology of the Choma-Kalomo block (Zambia) and geological implications. Abstracts volume, 20th Colloquium of African Geology, Orléans
- Cailteux JLH (1994) Lithostratigraphy of the Neoproterozoic Shaba-type (Zaire) Roan Supergroup and metallogenesis of associated stratiform mineralization. *J Afr Earth Sc* 19(4):279–301
- Cailteux J, Putter TD (2019) The Neoproterozoic Katanga Supergroup (D. R. Congo): state-of-the-art and revisions of the lithostratigraphy, sedimentary basin and geodynamic evolution. *J Afr Earth Sc* 150:522–531
- Cailteux JLH, Kampunzu AB, Lerouge C, Kaputo AK, Milesi JP (2005) Genesis of sediment-hosted stratiform copper–cobalt deposits, central African Copperbelt. *J Afr Earth Sc* 42(1–5):134–158
- Cailteux JLH, Kampunzu AB, Lerouge C (2007) The Neoproterozoic Mwashya-Kansuki sedimentary rock succession in the Central African Copperbelt, its Cu–Co mineralisation, and regional correlations. *Gondwana Res* 11(3):414–431
- Chappell BW, White AJR (1992) I- and S-type granites in the Lachlan Fold Belt. *Trans R Soc Edinburgh: Earth Sci* 83:1–26
- Chiu HY, Chung SL, Wu FY, Liu D, Liang YH, Lin JJ, Yoshiyukilizuka XLW, Wang YB, Chu MF (2009) Zircon U-Pb and Hf isotopic constraints from eastern Transhimalayan batholiths on the pre-collisional magmatic and tectonic evolution in southern Tibet. *Tectonophysics* 477(1–2):3–19
- Clemens JD (2003) S-type granitic magmas-petrogenetic issues, models and evidence. *Earth-science reviews*, 61, 1–18.
- Collins WJ, Beams SD, White AJR, Chappell BW (1982) Nature and origin of A-type granites with particular reference to southeastern Australia. *Contrib Miner Petrol* 80(2):189–200
- Condie KC (2005) TTGs and adakites: are they both slab melts? *Lithos* 80(1–4):33–44
- Corfu F, Hanchar JM (2003) Atlas of zircon textures. *Rev Miner Geochem* 53(1):469–500
- Cornell DH, Humphreys H, Theart HFJ, Scheepers DJ (1992) A collision-related pressure-temperature-time path for Prieska Copper Mine, Namaqua-Natal tectonic Province, South Africa. *Precambrian Res* 59(1–2):43–71
- Cosi M, De Bonis A, Goso G, Hunziker J, Martinotti G, Moratto S, Robert JP, Ruhlman F (1992) Late Proterozoic thrust tectonics, high-pressure metamorphism and uranium mineralization in the Domes area, Lufilian Arc, northwestern Zambia. *Precambrian Res* 58(1–4):215–240
- De Swardt AMJ, Gerrard P, Simpson J (1965) Major zones of transcurrent dislocation and superposition of orogenic belts in part of Central Africa. *Geol Soc Am Bullet* 76(1):89–102
- De Waele B, Kampunzu AB, Mapani B, Tembo F (2006) The Mesoproterozoic Irumide Belt of Zambia. *J Afr Earth Sc* 46:36–70
- De Waele B, Fitzsimons I, Wingate M, Tembo F, Mapani B, Belousova E (2009) The geochronological framework of the Irumide Belt: a prolonged crustal history along the margin of the Bangweulu Craton. *Am J Sci* 309(2):132–187
- Debruyne D, Hulsbosch N, Van Wilderode J, Balcaen L, Vanhaecke F, Muchez P (2015) Regional geodynamic context for the Mesoproterozoic Kibara Belt (KIB) and the Karagwe-Ankole Belt:

- evidence from geochemistry and isotopes in the KIB. *Precambr Res* 264:82–97
- Dirks PHGM, Sithole TA (1999) Eclogites in the Makuti gneisses of Zimbabwe: implications for the tectonic evolution of the Zambezi belt in Southern Africa. *J Metamorph Geol* 17:593–612
- Dokuz A (2011) A slab detachment and delamination model for the generation of Carboniferous high-potassium I-type magmatism in the Eastern Pontides, NE Turkey: the Köse composite pluton. *Gondwana Res* 19(4):926–944
- Dong YP, Zhang GW, Neubauer F, Liu XM, Hauzenberger C, Zhou DW, Li W (2011) Syn- and post-collisional granitoids in the Central Tianshan orogen: geochemistry, geochronology and implications for tectonic evolution. *Gondwana Res* 20(2–3):568–581
- Eby GN (1990) The A-type granitoids: A review of their occurrence and chemical characteristics and speculations on their petrogenesis. *Lithos* 26(1):115–134
- Eglinger A, André-Mayer AS, Vanderhaeghe O (2013) Geochemical signatures of uranium oxides in the Lufilian belt: from unconformity-related to syn-metamorphic uranium deposits during the Pan-African orogenic cycle. *Ore Geol Rev* 54:197–213
- Eglinger A, Vanderhaeghe O, André-Mayer AS, Goncalves P, Zeh A, Durand C, Deloule E (2016) Tectono-metamorphic evolution of the internal zone of the Pan-African Lufilian orogenic belt (Zambia): implications for crustal reworking and syn-orogenic uranium mineralizations. *Lithos* 240–243:167–188
- El Desouky HA, Muchez P, Cailteux J (2009) Two Cu–Co sulfide phases and contrasting fluid systems in the Katanga Copperbelt, Democratic Republic of Congo. *Ore Geol Rev* 36(4):315–332
- Fernandez-Alonso M, Cutten H, De Waele B, Tack L, Tahon A, Baudet D, Barritt SD (2012) The Mesoproterozoic Karagwe-Ankole Belt (formerly the NE Kibara Belt): the result of prolonged extensional intracratonic basin development punctuated by two short-lived far-field compressional events. *Precambr Res* 216:63–86
- Foerster HJ, Tischendorf G, Trumbull RB (1997) An evaluation of the Rb vs. (Y+Nb) discrimination diagram to infer tectonic setting of silicic igneous rocks. *Lithos* 40:261–293
- Gao JF, Lu JJ, Lai MY, Lin YP, Pu W (2003) Analysis of trace elements in rock samples using HR-ICPMS. *J Nanjing Univ (Nat Sci)* 39:844–850 in Chinese with English abstract
- Goldstein SL, O’Nion RK, Hamilton PJ (1984) A Sm-Nd isotopic study of atmospheric dusts and particulates from major river system. *Earth Planet Sci Lett* 70(2):221–236
- Goodge JW, Vervoort JD (2006) Origin of Mesoproterozoic A-type granites in Laurentia: Hf isotope evidence. *Earth Planet Sci Lett* 243:711–731
- Griffin WL, Pearson NJ, Belousova E, Jackson SE, Van Achterbergh E, O'Reilly SY, Shee SR (2000) The Hf isotope composition of cratonic mantle: LAM-MC-ICPMS analysis of zircon megacrysts in kimberlites. *Geochim Acta* 64(1):133–147
- Griffin WL, Jackson SE, Pearson NJ, O'Reilly SY, Xu X, Zhou X (2002) Zircon chemistry and magma mixing, SE China: in-situ analysis of Hf isotopes Tonglu and Pingtan Igneous Complexes. *Lithos* 61(3–4):237–269
- Gutzmer J, Beukes NJ, Pickard A, Barley ME (2000) 1170 Ma SHRIMP age for Koras Group bimodal volcanism, northern Cape Province[J]. *S Afr J Geol* 103(1):32–37
- Hamilton PJ, O’Nions RK, Bridgewater D, Nutman A (1983) Sm-Nd studies of Archaean metasediments and metavolcanics from West Greenland and their implications for the Earth’s early history. *Earth Planet Sci Lett* 62(2):263–272
- Hanson RE, Wilson TJ, Brueckner HK, Onstott TC, Wardlaw MS, Johns CC, Hardcastle KC (1988) Reconnaissance geochronology, tectonothermal evolution, and regional significance of the middle proterozoic choma-kalomo block, Southern Zambia. *Precambrian Res* 42(1–2):39–61
- Hanson RE, Wardlaw MS, Wilson TJ, Mwale G (1993) U-Pb zircon ages from the Hook Granite Massif and Mwembeshi dislocation: constraints on Pan-African deformation and transcurrent shearing in Central Zambia. *Precambr Res* 63:189–209
- Hanson RE, Wilson TJ, Munyanyiwa H (1994) Geologic evolution of the Neoproterozoic Zambezi orogenic belt in Zambia. *J Afr Earth Sc* 18(2):135–150
- Hanson RE, Martin MW, Bowring SA, Munyanyiwa H (1998) U-Pb zircon age for the Umkondo dolerites, eastern Zimbabwe: 1.1 Ga large igneous province in southern Africa-East Antarctica and possible Rodinia correlations. *Geology* 26:1143–1146
- Hegenberger W, Burger AJ (1985) The Oorlogsende porphyry member, South West Africa/Namibia: its age and regional setting. *Commun Geol Surv Namibia* 1:23–29
- Heilimo E, Elburg MA, Andersen T (2014) Crustal growth and reworking during Lapland-Kola orogeny in northern Fennoscandia: U-Pb and Lu-Hf data from the Nattanen and Litsa-Aragub-type granites. *Lithos* 205:112–126
- Hitzman MW, Selley D, Bull S (2010) Formation of sedimentary rock-hosted stratiform copper deposits through Earth history. *Econ Geol* 105(3):627–639
- Hoal BG, Heaman LM (1995) The Sinclair sequence: U-Pb age constraints from the Awasib mountain area. *Commun Geol Surv Namibia* 10:83–91
- Hoskin PWO, Schaltegger U (2000) The composition of zircon and igneous and metamorphic petrogenesis. *Rev Mineral Geochem* 53(1):27–62
- John T, Schenk V, Haase K, Scherer R, Tembo F, (2003) Evidence for a Neoproterozoic ocean in South-central Africa from mid-oceanic ridge-type geochemical signatures and pressure–temperature estimates of Zambian eclogites. *Geology* 31(3):243–246
- John T, Schenk V, Mezger K, Tembo F (2004) Timing and PT evolution of whiteschist metamorphism in the Lufilian arc-Zambezi belt orogen (Zambia): implications for the assembly of Gondwana. *J Geol* 112:71–90
- Johnson SP, Rivers T, De Waele B (2005) A review of the Mesoproterozoic to early Palaeozoic magmatic and tectonothermal history of south-central Africa: implications for Rodinia and Gondwana. *J Geol Soc* 162(3):433–450
- Kampunzu AB, Cailteux J (1999) Tectonic evolution of the Lufilian arc Central Africa Copperbelt during Neoproterozoic Pan-African orogenesis. *Gondwana Res* 2:135–150
- Kampunzu AB, Akanyang P, Mapeo RBM, Modie BN, Wendorff M (1998) Geochemistry and tectonic significance of the Mesoproterozoic Kgwebe metavolcanic rocks in northwest Botswana: implications for the evolution of the Kibaran Namaqua-Natal belt[J]. *Geol Mag* 135(5):669–683
- Kampunzu AB, Tembo F, Matheis G, Kapenda D, Huntsman-Mapila P (2000) Geochemistry and tectonic setting of mafic igneous units in the Neoproterozoic Katangan Basin, Central Africa: implications for Rodinia break-up. *Gondwana Res* 3(2):125–153
- Karsli O, Caran S, Dokuz A, Çoban H, Chen B, Kandemir R (2012) A-type granitoids from the Eastern Pontides, NE Turkey: records for generation of hybrid A-type rocks in a subduction-related environment. *Tectonophysics* 530–531:208–224
- Katongo C, Koller F, Kloetzli U, Koeberl C, Tembo F, De Waele B (2004) Petrography, geochemistry, and geochronology of granitoid rocks in the Neoproterozoic-Paleozoic Lufilian-Zambezi belt, Zambia: implications for tectonic setting and regional correlation. *J Afr Earth Sc* 40(5):219–244
- Kemp A, Hawkesworth C (2003) Granitic perspective on the generation and secular evolution of the continental crust. *Treatise on Geochemistry* 3(6):349–410
- Key RM, Mapeo R (1999) The Mesoproterozoic history of Botswana and the relationship of the NW Botswana Rift to Rodinia. *Episodes* 22(2):118–122

- Key RM, Liyungu AK, Njam FM, Somwe V, Banda J, Mosley PN, Armstrong RA (2001) The western arm of the Lufilian Arc in NW Zambia and its potential for copper mineralization[J]. *J Afr Earth Sc* 33(3–4):503–528
- King PL, White AJR, Chappell BW, Allen CM (1997) Characterization and origin of aluminous A-type granites from the Lachlan Fold Belt, Southeastern Australia. *J Petrol* 38:371–391
- Kinzler RJ (1997) Melting of mantle peridotite at pressures approaching the spinel to garnet transition: application to mid-ocean ridge basalt petrogenesis. *J Geophys Res: Solid Earth* 102(B1):853–874
- Klerkx J, Liégeois JP, Lavreau J, Claessen W (1987) Crustal evolution of the northern Kibaran belt, eastern and central Africa[J]. *Proterozoic Lithospheric Evol* 17:217–233
- Kokonyangi J, Armstrong R, Kampunzu AB, Yoshida M, Okudaira T (2004) U-Pb zircon geochronology and petrology of granitoids from Mitwaba (Katanga, Congo): implications for the evolution of the Mesoproterozoic Kibaran Belt. *Precambr Res* 132(1–2):79–106
- Kokonyangi J, Okudaira T, Kampunzu AB, Yoshida M (2001) Geological Evolution of the Kibarides Belt, Mitwaba, Democratic Republic of Congo, Central Africa. *Gondwana Res* 4(4):663–664
- Kokonyangi JW, Kampunzu AB, Armstrong R, Yoshida M, Okudaira T, Arima M, Ngulube DA (2006) The Mesoproterozoic Kibaride Belt (Katanga, SE DR Congo). *J Afr Earth Sc* 46(1–2):1–35
- Li XH, Li ZX, Li WX, Liu Y, Yuan C, Wei GJ, Qi CS (2007) U-Pb zircon, geochemical and Sr-Nd-Hf isotopic constraints on age and origin of Jurassic Iand A-type granites from central Guangdong, SE China: a major igneous event in response to foundering of a subducted flat-slab? *Lithos* 96:186–204
- Liu YS, Hu ZC, Gao S, Günther D, Xu J, Gao CG, Chen HH (2008) In situ analysis of major and trace elements of anhydrous minerals by LA-ICP-MS without applying an internal standard. *Chem. Geol.* 257(1–2):34–43
- Liu S, Hu RZ, Gao S, Feng CX, Huang ZL, Lai SC, Yuan HL, Liu XM, Coulson IM, Feng GY, Wang T, Qi YQ (2009) U-Pb zircon, geochemical and Sr-Nd-Hf isotopic constraints on the age and origin of Early Palaeozoic I-type granite from the Tengchong-Baoshan Block, Western Yunnan Province, SW China. *J Asian Earth Sci* 36(2–3):168–182
- Liu YS, Gao S, Hu ZC, Gao CG, Zong KQ, Wang DB (2010a) Continental and oceanic crust recycling-induced melt-peridotite interactions in the Trans-North China Orogen: U-Pb dating, Hf isotopes and trace elements in zircons from mantle xenoliths. *J Petrol* 51(1&2):537–571
- Liu YS, Hu ZC, Zong KQ, Gao CG, Gao S, Xu J, Chen HH (2010b) Reappraisal and refinement of zircon U-Pb isotope and trace element analyses by LA-ICP-MS. *Chin Sci Bull* 55(15):1535–1546
- Liu L, Qiu JS, Zhao JL, Yang ZL (2014) Geochronological, geochemical, and Sr-Nd-Hf isotopic characteristics of Cretaceous monzonitic plutons in western Zhejiang Province, Southeast China: new insights into the petrogenesis of intermediate rocks. *Lithos* 196–197:242–260
- Liu CF, Zhang J, Tang L, Yang F, Guo JT, Zhou C, Cai ZW, Bian XL (2019) Detrital zircon U-Pb geochronology and provenance of the Neoproterozoic Lower Roan Group, Chambishi Basin, North-eastern Zambia: Implication for rift evolution of the Congo Craton. *Geol J* 55(2):1245–1261
- Liu CF, Zhang J, Tang L, Yang F, Guo JT, Zhou C, Cai ZW, Bian XL (2020) Detrital zircon U-Pb geochronology and provenance of the Neoproterozoic Lower Roan Group, Chambishi Basin, North-eastern Zambia: implication for rift evolution of the Congo Craton. *Geol J* 55(2):1245–1261
- Loiselle MC, Wones DR (1979) Characteristics and origin of anorogenic granites. *Abstracts with Programs - Geological Society of America* 12(7):468
- Ludwig KR (2003) User's Manual for Isoplot 3.00, a Geochronological Toolkit for Microsoft Excel. Geochronological Center, Special Publication No. 4, Berkeley, 25–32.
- Lugmair GW, Hart K (1978) Lunar initial  $^{143}\text{Nd}/^{144}\text{Nd}$ : differential evolution of the lunar crust and mantle. *Earth Planet Earth Planet Sci Lett* 39(3):349–357
- Maniar PD, Piccoli PM (1989) Tectonic discrimination of granitoids. *Geol Soc Am Bull* 101(5):635–643
- Mark G (1999) Petrogenesis of Mesoproterozoic K-rich granitoids, southern Mt Angelay igneous complex, Cloncurry district, northwest Queensland. *Aust J Earth Sci* 46:933–949
- Martin H, Bonin B, Capdevila R, Jahn BM, Lameyre J, Wang Y (1994) The Kuiqi peralkaline granitic complex (SE China): petrology and geochemistry. *J Petrol* 35:983–1015
- Master S, Rainaud C, Armstrong RA, Phillips D, Robb LJ (2005) Provenance ages of the Neoproterozoic Katanga Supergroup (Central African Copperbelt), with implications for basin evolution. *J Afr Earth Sc* 42(1–5):41–60
- Middlemost EAK (1994) Naming materials in the magma/igneous rock system. *Earth Sci Rev* 37:215–244
- Muchez P, Vanderhaeghen P, El Desouky H, Schneider J, Boy A, Dewaele S, Cailteux J (2008) Anhydrite pseudomorphs and the origin of stratiform Cu-Co ores in the Katangan Copperbelt (Democratic Republic of Congo). *Miner Deposita* 43(5):575
- Naydenov KV, Lehmann J, Saalmann K, Milani L, Kinnaird JA, Charlesworth G, Rankin W (2014) New constraints on the Pan-African Orogeny in Central Zambia: a structural and geochronological study of the Hook Batholith and the Mwenbeshi Zone. *Tectonophysics* 637:80–105
- Nesbitt H, Young GM (1982) Early Proterozoic climates and plate motions inferred from major element chemistry of lutites. *Nature* 299:715–717
- Patchett PJ, Kouvo O, Hedge CE, Tatsumoto M (1982) Evolution of continental crust and mantle heterogeneity: evidence from Hf isotopes. *Contrib Miner Petrol* 78(3):279–297
- Patiño Douce AE (1997) Generation of metaluminous A-type granites by low-pressure melting of calc-alkaline granitoids. *Geology* 25:743–746
- Patiño Douce AE, Beard JS (1995) Dehydration-melting of biotite gneiss and quartz amphibolite from 3 to 15 kbar. *J Petrol* 36:707–738
- Pearce JA, Harris NBW, Tindle AG (1984) Trace element discrimination diagrams for the tectonic interpretation of granitic rocks. *J Petrol* 25:956–983
- Pfurr N, Ahrendt H, Hansen BT, Weber K (1991) U-Pb and Rb-Sr isotopic study of granitic gneisses and associated metavolcanic rocks from the Rostock massifs, southern margin of the Damara Orogen: implications for lithostratigraphy of this crustal segment. *Commun Geol Surv Namibia* 7:35–48
- Polat A, Hofmann AW (2003) Alteration and geochemical patterns in the 3.7–3.8 Ga Isua greenstone belt West Greenland. *Precambr Res* 126(3–4):197–218
- Porada H (1989) Pan-African rifting and orogenesis in southern to equatorial Africa and eastern Brazil. *Precambr Res* 44(2):103–136
- Porada H, Berhorst V (2000) Towards a new understanding of the Neoproterozoic-Early Palaeozoic Lufilian and northern Zambezi belts in Zambia and the Democratic Republic of Congo. *J Afr Earth Sc* 30:727–771
- Rainaud C, Master S, Armstrong RA, Robb LJ (2003) A cryptic Mesoarchaean terrane in the basement to the Central African Copperbelt. *J Geol Soc* 160(1):11–14

- Rainaud C, Master S, Armstrong RA, Robb LJ (2005) Geochronology and nature of the Palaeoproterozoic basement in the Central African Copperbelt (Zambia and the Democratic Republic of Congo), with regional implications. *J Afr Earth Sc* 42(1–5):1–31
- Rapp RP, Watson EB (1995) Dehydration melting of metabasalt at 8–32 kbar: implications for continental growth and crust-mantle recycling. *J Petrol* 36(4):891–931
- Ren YW, Zhang JH, Tian H, Wang HC, Shi JR, Chang QS (2022) Zhang K (2022) Petrogenesis and geodynamic settings of monzonitic granite at the end of the Neoarchean in Tianshen-Huai'an area. *N China Geology* 45(2):76–86
- Robb LJ, Armstrong RA, Waters DJ (1999) The history of granulite-facies metamorphism and crustal growth from single zircon U-Pb geochronology: Namaqualand, South Africa. *J Petrol* 40(12):1747–1770
- Roberts MP, Clemens JD (1993) Origin of high-potassium, calc-alkaline, I-type granitoids. *Geology* 21:825–828
- Rubatto D (2017) Zircon: the metamorphic mineral. *Rev Mineral Geochim* 83:261–295
- Sarjoughian F, Kananian A, Haschke M, Ahmadian J (2016) Transition from I-type to A-type magmatism in the Sanandaj-Sirjan Zone, NW Iran: an extensional intra-continental arc. *Geol J* 51(3):387–404
- Scherer E, Munker C, Mezger K (2001) Calibration of the lutetium-hafnium clock. *Science* 293:683–687
- Schwartz MO, Kwok YY, Davis DW, Akangyang p, (1996) Geology, geochronology and regional correlation of the Ghanzi Ridge, Botswana. *S Afr J Geol* 99(3):245–250
- Selley D, Broughton D, Scott RJ, Hitzman M, Bull SW, Large RR, Pollington N (2005) A new look at the geology of the Zambian Copperbelt. *Econ Geol* 100:965–1000
- Shang C, Satir M, Nsifa E, Liégeois JP, Siebel W TH (2007) Archaean high-K granitoids produced by remelting of earlier tonalite-trondhjemite-granodiorite (TTG) in the Sangmelima region of the Ntem complex of the Congo craton, southern Cameroon. *Int J Earth Sci* 96:817–841
- Singletary SJ, Hanson RE, Martin MW, Crowley JL, Bowring SA, Key RM, Ramokate LV, Direng BB, Krol MA (2003) Geochronology of basement rocks in the Kalahari Desert, Botswana, and implications for regional Proterozoic tectonics. *Precambr Res* 121(1–2):47–71
- Sisson TW, Ratajeski K, Hankins WB, Glazner AF (2005) Voluminous granitic magmas from common basaltic sources. *Contrib Miner Petrol* 148(6):635–661
- Skjerlie KP, Johnston AD (1993) Fluid-absent melting behavior of an F-rich tonalitic gneiss at mid-crustal pressures: implications for the generation of anorogenic granites. *J Petrol* 34(4):785–815
- Stern CR, Kilian R (1996) Role of the subducted slab, mantle wedge and continental crust in the generation of adakites from the Andean Austral Volcanic Zone. *Contrib Miner Petrol* 123(3):263–281
- Streckeisen A (1976) To each plutonic rock its proper name. *Earth Sci Rev* 12:1–33
- Sun SS, McDonough WF (1989) Chemical and isotopic systematics of oceanic basalts: implications for mantle composition and processes. *Geol Soc* 42(1):313–345 London, Special Publications
- Sun HW, Ren JP, Wang J, Gu AL, Wu XY, He FQ, Zuo LB, Mukofu C, Dokwe AP, Chikambwe E, Liu ZJ, Xing S (2021) Age and geochemistry of the granitoids from the Lunte area, Northeastern Zambia: implications for magmatism of the Columbia supercontinent, China. *Geology* 4(4):658–672
- Tack L, Wingate MTD, De Waele B, Meert J, Belousova E, Griffin B, Tahon A, Fernandez-Alonso M (2010) The 1375Ma “Kibaran event” in Central Africa: prominent emplacement of bimodal magmatism under extensional regime. *Precambr Res* 180(1–2):63–84
- Unrug R (1983) The Lufilian Arc: a microplate in the Pan-African collision zone of the Congo and the Kalahari cratons. *Precambr Res* 21(3–4):181–196
- Vinyu ML, Hanson RE, Martin MW, Bowring SA, Jelsma HA, Krol MA, Dirks PHGM (1999) U-Pb and  $^{40}\text{Ar}/^{39}\text{Ar}$  geochronological constraints on tectonic evolution of the eastern part of the Zambezi orogenic belt, northeast Zimbabwe. *Precambr Res* 98:67–82
- Watkins J, Clemens J, Treloar P (2007) Archaean TTGs as sources of younger granitic magmas: melting of sodic metatonalites at 0.6–1.2 GPa. *Contrib Miner Petrol* 154:91–110
- Watson EB, Harrison TM (1983) Zircon saturation revisited: temperature and composition effects in a variety of crustal magma types. *Earth Planet Sci Lett* 64(2):295–304
- Whalen JB, Currie KL, Chappell BW (1987) A-type granites: geochemical characteristics, discrimination and petrogenesis. *Contrib Miner Petrol* 95(4):407–419
- Wingate MTD (2001) SHRIMP baddeleyite and zircon ages for an Umkondo dolerite sill, Nyanga Mountains, Eastern Zimbabwe. *S Afr J Geol* 104(1):13–22
- Witt WK, Hagemann SG, Villanes C (2014) Geochemistry and geology of spatially and temporally associated calc-alkaline (I-type) and K-rich (A-type) magmatism in a Carboniferous continental arc setting, Pataz gold-mining district, northern Peru. *Aust J Earth Sci* 61(1):17–42
- Wu FY, Lin JQ, Wilde SA, Yang JH (2005) Nature and significance of the Early Cretaceous giant igneous event in eastern China. *Earth Planet Sci Lett* 233(1–2):103–119
- Xu KK, Sun K, He SF, Gong PH, Zhang H, Lu YG (2021) Detrital zircon U-Pb dating of the garnet mica schist and its geological implications in the Solwezi area, Northwestern Zambia. *N China Geol* 44(3):3 in Chinese with English abstract
- Yuan HL, Gao S, Liu XM, Li HM (2004) Accurate U-Pb age and trace element determination of zircon by laser ablation-inductively coupled plasma mass spectrometry. *Geostand Geoanal Res* 28(3):353–370
- Zhang Q, Jin WJ, Wang YL, Li CD, Wang Y, Jia XQ (2006) A model of delamination of continental lower crust. *Acta Petrol Sin* 22(2):265–276
- Zhang Q, Jin WJ, Li CD, Wang Y, Wang YL (2011) Granitic rocks and their formation depth in the crust. *Geotecton Metallog* 35(2):259–269 in Chinese with English abstract
- Zhao XF, Zhou MF, Li JW, Wu FY (2008) Association of Neoproterozoic A- and I-type granites in South China: implications for generation of A-type granites in a subduction-related environment. *Chem Geol* 257:1–15
- Zhao JL, Qiu JS, Liu L, Wang RQ (2016) The Late Cretaceous I- and A-type granite association of southeast China: implications for the origin and evolution of post-collisional extensional magmatism. *Lithos* 240:16–33
- Zhao J, Zhang C, Guo X, Liu X (2018) The late-Paleoproterozoic I-and A-type granites in Lüliang Complex, North China Craton: new evidence on post-collisional extension of Trans-North China Orogen. *Precambr Res* 318:70–88

Springer Nature or its licensor (e.g. a society or other partner) holds exclusive rights to this article under a publishing agreement with the author(s) or other rightsholder(s); author self-archiving of the accepted manuscript version of this article is solely governed by the terms of such publishing agreement and applicable law.